Mixed-integer, multi-objective layerwise optimization of variable-stiffness composites with gaps and overlaps

Structural and Multidisciplinary Optimization (2025) 68:107
https://doi.org/10.1007/s00158-025-04043-6

RESEARCH PAPER

Mixed-integer, multi-objective layerwise optimization of variable-stiffness composites with gaps and overlaps

D. Zamani[1] · **A. Racionero Sánchez-Majano**[1,2] · **A. Pagani**[1]

Received: 16 December 2024 / Revised: 8 April 2025 / Accepted: 13 May 2025 / Published online: 14 June 2025

Abstract
Automated fiber placement (AFP) has made it possible to vary the steering angle along curvilinear fiber paths, thus improving mechanical performance compared to traditional composite materials. Variable-angle tow (VAT) or variable-stiffness composites (VSC) have been developed to enhance structural performance through material optimization and effective load-bearing configurations. These advanced materials contribute to achieving optimal performance while reducing the weight of aircraft and aerospace structures. However, defects such as gaps and overlaps may arise during the manufacturing process. Whereas the latter increases local thickness, the former causes resin-rich areas within each lamina. The mass and structural optimization of this kind of structure is challenging as it combines discrete and continuous design variables, namely the number of layers and the fiber path parameters, where the latter influence the presence of defects within the laminate. To tackle this optimization problem, this work proposes a mixed-integer strategy specifically designed to select the least-weight design of a VAT laminate while also fulfilling requirements on the first natural frequency and buckling load while accounting for the manufacturing signature of the AFP process. This study combines the Carrera unified formulation (CUF) and the defect layer method (DLM) to model the VAT laminates and incorporating the fabrication defects. The research has two main aims: (i) to determine the minimum number of layers required to satisfy the fundamental frequency and buckling constraints, considering the manufacturing signature, and (ii) to investigate the influence of the selected structural theory on the optimal design solutions.

Keywords Variable stiffness composites · Variable-angle tow · Unified formulation · Structural optimization.

1 Introduction

Recent advancements in composite manufacturing, such as automated fiber placement (AFP) (Rousseau et al. 2018; Zhang et al. 2020; Brasington et al. 2021), automated tape laying (ATL) (Lukaszewicz et al. 2012), and continuous tow shearing (CTS) (Kim et al. 2012, 2014), have enabled the fabrication of variable-stiffness composites (VSC), also known as variable angle tow (VAT), which feature curvilinear fiber paths and spatially varying stiffness. While these laminates offer enhanced mechanical performance, their potential is limited by manufacturing-induced defects. In AFP, gaps and overlaps are the most common defects (Heinecke and Willberg 2019); the former creates resin-rich areas, while the latter causes local thickness increases (Harik et al. 2018). Several numerical methods have been developed to model such imperfections. Blom et al. (2009) proposed a defect identification approach based on refined two-dimensional (2D) finite element (FE) meshes, though at high computational cost. To reduce this burden, the defect layer method (DLM) was introduced by Fayazbakhsh et al. (2013), assigning local properties based on gap and overlap volume fractions. Ghayour et al. (2021) further extended this strategy with the multiscale Induced DLM, introducing a gap percentage metric to embed defects without altering the mesh. Experimental studies by Nguyen et al. (2019a, 2019b) showed that gaps degrade compressive strength, whereas

Responsible editor: Kai James

✉ A. Pagani
alfonso.pagani@polito.it

[1] MUL 2 Lab, Department of Mechanical and Aerospace Engineering, Politecnico di Torino, Corso Duca degli Abruzzi 24, 10129 Turin, Italy

[2] Department of Aerospace Engineering, Universidad Carlos III de Madrid, Av. de la Universidad 30, 28911 Leganés-Madrid, Spain

overlaps enhance tensile performance with minimal impact on compression. Akbarzadeh et al. (2014) investigated VAT plates with embedded defects and highlighted that discrepancies between equivalent-single-layer (ESL) theories, such as the classical laminate theory (CLPT) and third-order shear deformation theory (TSDT), become significant in thick laminates due to their limited ability to capture transverse shear effects.

Unlike ESL models based on classical theories, layerwise (LW) models assign independent displacement fields to each layer, enforcing interlaminar continuity to capture through-thickness behavior. Demasi et al. (2017) applied LW theories to VAT laminates using the Carrera unified formulation (CUF), enabling different orders of expansion. CUF was also used by Viglietti et al. (2019) to investigate free vibration problems through variable kinematic models. Sánchez-Majano et al. (2021) compared ESL and LW approaches for VAT shells, showing that only LW models accurately captured shear stresses. Pagani et al. (2022) extended CUF-based LW modeling to nonlinear dynamic analyses of VAT plates. LW models have been employed at smaller scales to study the mesoscale and microscale response of VSCs under uncertainty. In particular, in-plane waviness and fiber volume fraction variations were modeled through stochastic LW fields to assess their impact on buckling and fiber-matrix stress states (see Sáanchez-Majano et al. 2021b; Pagani et al. 2023).

VSCs offer a significantly broader design space than traditional laminates but introduce non-uniform stiffness distributions that increase computational demands (Gurdal and Olmedo 1993); thus, efficient optimization frameworks are needed. Several authors have tackled this challenge from different perspectives. Ding et al. (2022) integrated Tsai–Wu strength criteria and manufacturing rules into a gradient-based optimization via radial basis function parameterization. Arian Nik et al. (2012, 2014) proposed a multi-objective approach combining surrogate models for in-plane stiffness and buckling with evolutionary algorithms. Groh and Weaver (2015) optimized VAT laminates fabricated via CTS using a genetic algorithm (GA) coupled with pattern search, achieving substantial weight savings. Racionero Sánchez-Majano and Pagani (2023) leveraged CUF-based surrogate models within a GA to optimize buckling and natural frequency, highlighting the role of structural theory fidelity. Although many works focus on continuous design variables (e.g., fiber orientations), several studies emphasize that fully exploiting the mechanical performance of variable-stiffness composites also requires treating the number of plies and ply thicknesses as discrete design variables. The number of plies is naturally an integer parameter, and ply thicknesses often need to be integral multiples of a baseline thickness to adhere to manufacturing constraints. If these variables are merely relaxed to continuous values, the resulting designs may violate production requirements or deviate significantly from the actual optimum. In this context, An et al. (2025) propose an integrated optimization framework for ply number, layer thickness, and fiber angles. Their findings demonstrate that ignoring such discrete constraints can lead to suboptimal or infeasible solutions, reinforcing the necessity for a mixed-integer approach in variable-stiffness composite optimization. Further evidence of the importance of integer-based formulations for laminate design is provided by Borwankar et al. (2022, 2023). These studies employ mixed-integer programming (MIP) to manage discrete ply orientations and thicknesses. By formulating lamination parameters and failure constraints in terms of binary decision variables, their approach efficiently addresses combinatorial complexity while capturing critical manufacturing requirements such as distinct ply thicknesses or material choices. In addition, Ntourmas et al. (2021) addressed the manufacturability of stacking sequences and blending through MIP, enabling the generation of discrete stacking solutions that respect structural and fabrication constraints.

As noted by Lozano et al. (2015), the advancement of optimization tools capable of handling manufacturing imperfections is essential for the success of advanced tailoring strategies. Several studies have explicitly integrated defects into the optimization process in this context. Carvalho et al. (2022) maximized the fundamental frequency by adjusting lamination angles while modeling gaps through a modified rule of mixtures and solving the problem with GA. Tian et al. (2019) proposed a framework that defines fiber paths as continuous functions and derives gaps, overlaps, and curvature constraints based on local fiber angle variation. Vijayachandran et al. (2020) coupled a GA with an artificial neural network (ANN) surrogate to optimize steered fiber paths under compressive loads, showing improved buckling performance over traditional straight-fiber layouts. At a multiscale level, Montemurro and Catapano (2017) developed the MS2LOS strategy to embed manufacturability constraints—such as tow curvature limits—directly within the first level of a hierarchical optimization. A similar approach was employed by Izzi et al. (2021) for the mass and strength optimization of VAT laminates. Finally, Pagani et al. (2024a, 2024b) proposed a surrogate-based optimization framework incorporating gaps and overlaps into CUF.

This study introduces a novel layerwise optimization framework for tow-steered laminates using a discrete, mixed-integer, multi-objective approach. This framework minimizes structural mass while maximizing either fundamental frequency or buckling load. Its core innovation lies in the layer-level formulation, which handles the discontinuous response surfaces inherent to discrete ply optimization and, crucially, allows for the explicit modeling and integration of manufacturing defects specific to each ply directly within the optimization loop. This capability enables investigation into two key areas:

(i) the impact of AFP manufacturing constraints and defect characteristics on the minimum ply count needed to achieve performance targets and (ii) the influence of the selected structural theory on the optimal design when manufacturing imperfections are explicitly considered. CUF was adopted to systematically compare different structural models while preserving a consistent mesh and governing equation formulation.

The paper is organized as follows: Sect. 2 presents the main characteristics of VAT plates and the methodology for defect estimation and mapping. Section 3 introduces CUF and its application to free vibration and buckling analysis using unified finite elements. Section 4 details the mixed-integer multi-objective optimization framework. Section 5 discusses the optimization outcomes, and Sect. 6 summarizes the key findings.

2 Tow-steered plates

2.1 Fiber deposition modeling

In this manuscript, the expression of the linearly varying fiber orientation is taken from the work by Gürdal et al. (2008) and reads as follows:

$$\theta(x') = \phi + T_0 + \frac{(T_1 - T_0)}{d}|x'|. \tag{1}$$

With this expression, the local fiber orientation varies from T_0 at $x' = 0$ to T_1 at $x' = d$, being d the variation length from T_0 and T_1. The parameter ϕ represents the fiber path rotation angle and determines the axis along which the courses are laid, whether along the x-axis, y-axis, or a combination of both. In this regard, the stacking sequence of a VAT laminate is defined as $[\phi^1\langle T_0, T_1\rangle^1, \phi^2\langle T_0, T_1\rangle^2, \dots, \phi^n\langle T_0, T_1\rangle^n]$, being n the total number of layers. Note that the x' axis is defined as $x' = x\cos(\phi) + y\sin(\phi)$. Although d can assume any value, it is typically set to either the plate's semi-width, $a/2$, or semi-length, $b/2$, depending on whether $\phi = 0°$ or $\phi = 90°$, respectively, as illustrated in Fig. 1.

To represent the centerline of the fiber course, one needs to solve the following differential equation:

$$\frac{\mathrm{d}y}{\mathrm{d}x} = \tan(\theta) \tag{2}$$

which, in the case of linearly varying fiber path with $\phi = 0°$ and $d = a/2$, has the following solution:

$$y(x) = \begin{cases} \frac{a}{2(T_0 - T_1)}\left(\ln\left(\cos(T_0)\right) + \ln\left(\cos\left(-T_0 + 2T_1 + \frac{2(T_1 - T_0)}{a}x\right)\right)\right) & -a \le x \le -\frac{a}{2} \\ \frac{a}{2(T_1 - T_0)}\left(-\ln\left(\cos(T_0)\right) + \ln\left(\cos\left(T_0 + \frac{2(T_0 - T_1)}{a}x\right)\right)\right) & -\frac{a}{2} \le x \le 0 \\ \frac{a}{2(T_0 - T_1)}\left(-\ln\left(\cos(T_0)\right) + \ln\left(\cos\left(T_0 + \frac{2(T_1 - T_0)}{a}x\right)\right)\right) & 0 \le x \le \frac{a}{2} \\ \frac{a}{2(T_1 - T_0)}\left(\ln\left(\cos(T_0)\right) + \ln\left(\cos\left(-T_0 + 2T_1 + \frac{2(T_0 - T_1)}{a}x\right)\right)\right) & \frac{a}{2} \le x \le a \end{cases} \tag{3}$$

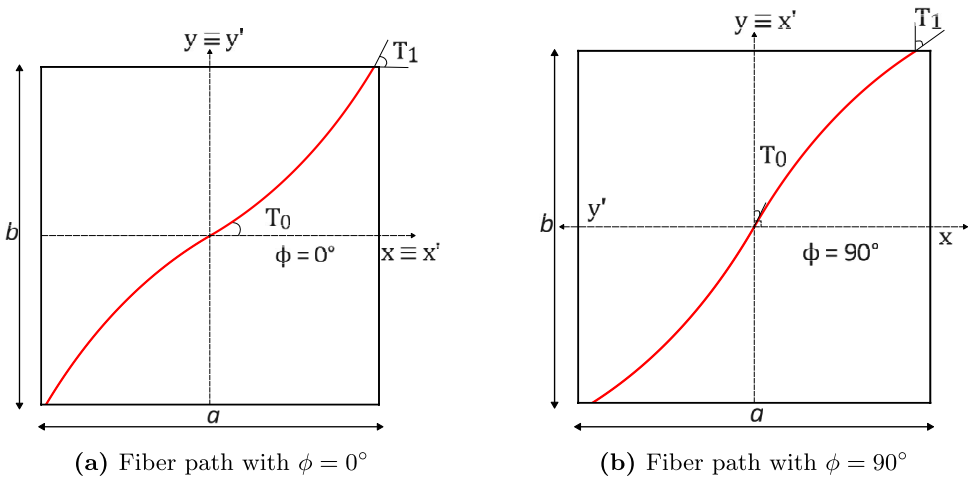

Fig. 1 Graphical representation of the parameters involved in a linearly varying fiber path for $\phi = 0°$ (left) and $\phi = 90°$ (right)

(a) Fiber path with $\phi = 0°$

(b) Fiber path with $\phi = 90°$

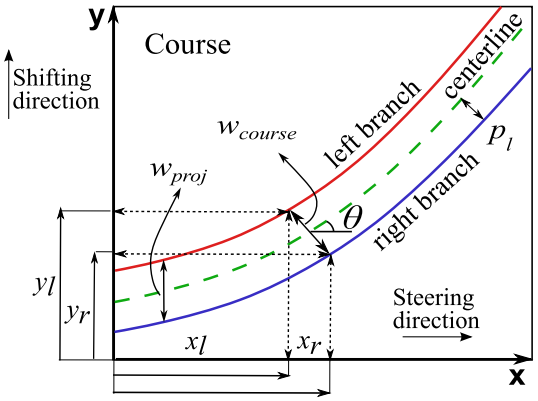

Fig. 2 Representation of the AFP parameters that define the centerline and the left and right course branches

Having the equations for the centerline, it is possible to generate the left and right branches of a fiber course at an appropriate distance by incorporating the AFP parameters that emulate the steering process, as illustrated in Fig. 2. A course consists of multiple tows, with the number of tows, N_t, determined by the AFP head's capacity. Most AFP machines can simultaneously lay down 8, 12, 16, 24, or 32 tows. Given that each tow has a fixed width, t_w, set to 3.125 mm in this document, the total width of a single course, w_{course}, can be calculated as $w_{\text{course}} = N_t t_w$, being 16 the number of tows considered in this manuscript. Once the AFP manufacturing parameters are established, the various fiber courses for each layer in the laminate are simulated using the geometric parameters depicted in Fig. 2. The expressions for the left and right branches are reported in Eq. (4). Specifically, x_l, y_l, x_r, and y_r represent the x and y coordinates of the left and right branches, respectively, and p_l is the semi-width of the course and is calculated as $0.5N_t t_w$:

$$\begin{aligned} \text{Left branch:} \quad & \begin{cases} x_l = x - p_l \sin\theta(x) \\ y_l = y + p_l \cos\theta(x) \end{cases} \\ \text{Right branch:} \quad & \begin{cases} x_r = x + p_l \sin\theta(x) \\ y_r = y - p_l \cos\theta(x) \end{cases} \end{aligned} \tag{4}$$

The work by Brooks and Martins (2018) established the manufacturing constraints to be considered in optimizing VAT structures. These limitations are related to the AFP machine. The one used in this study is the maximum allowed curvature, which in the case where $\phi = 0°$ is calculated as follows:

$$\kappa = \text{sgn}(x)\frac{2(T_1 - T_0)}{a}\cos\left((T_1 - T_0)\frac{x}{a/2} + T_0\right) \tag{5}$$

where sgn(·) denotes the sign function. In this manner, providing a set of T_0 and T_1, the local curvature of the fiber path is retrieved and must not exceed the maximum allowed curvature κ_{lim}, as shown in Eq. (6), where r_{min} denotes the minimum turning radius achievable by the AFP machine:

$$-\frac{1}{r_{\text{min}}} \leq \kappa \leq \frac{1}{r_{\text{min}}} \tag{6}$$

As illustrated in Fig. 2, when examining a generic fiber course, it is evident that the vertical projection of the course width decreases or increases depending on the fiber path angles T_0 and T_1. The projected width is calculated as

$$w_{\text{proj}} = \frac{w_{\text{course}}}{\cos\theta} \tag{7}$$

Steering fiber bands along a fixed direction and shifting the AFP head perpendicular to this direction to lay down the consecutive fiber course may result in gaps and/or overlaps. The occurrence of these defects depends on the combination of T_0 and T_1 angles and the selected deposition strategy, as summarized in Table 1. Two consecutive courses can be set to be tangent at the center or the edge of the plate. In this context, Fig. 3 illustrates the case of a $[\langle 0, 45\rangle]$ plate, where the tangency condition is applied at the edge and the center. When tangency is enforced at the edge, as seen in Fig. 3a, gaps appear at the center of the plate; conversely, when tangency is imposed at the center, overlaps occur at the plate edges, see Fig. 3b. Similarly, Fig. 4 shows a $[\langle 60, 30\rangle]$ plate with the same tangency conditions. In this case, the contact-at-the-center strategy results in gaps at the edges, as shown in Fig. 4a, while enforcing tangency at the edges produces overlaps at the center of the plate, see Fig. 4b.

Table 1 Type and location of defects based on fiber characteristics and manufacturing strategy

Condition	Tangency at the edge	Tangency at the center
$\lvert\cos(T_0)\rvert > \lvert\cos(T_1)\rvert$	Gap at center	Overlap at edges
$\lvert\cos(T_0)\rvert < \lvert\cos(T_1)\rvert$	Overlap at center	Gap at edges

A large presence of imperfections is observed in Figs. 3 and 4. It occurs because the width of each course is kept constant during the deposition process. To minimize the defect area, the course width must either decrease when a course intersects with the subsequent one or increase when it does not reach the edge of the previous course. This adjustment in course width is achieved by cutting a single tow and resuming its deposition, resulting in the formation of small triangular defect regions along the fiber path, as shown in Fig. 5. The deposition strategy modeled in this document simulates the correction process with a coverage parameter, establishing the degree of overlap permitted for each course. In particular, only gaps will occur with a coverage value equal to 0%, whereas with a

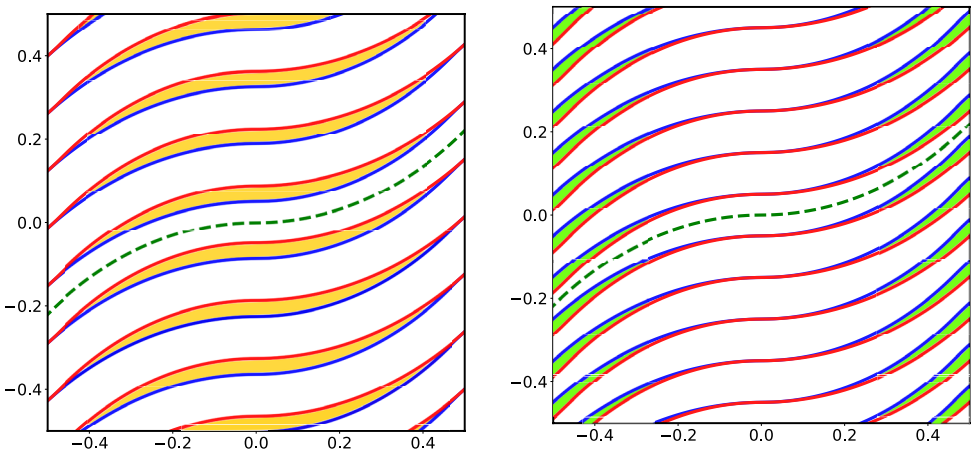

(a) $[\langle 0, 45\rangle]$ with complete gap **(b)** $[\langle 0, 45\rangle]$ with complete overlap

Fig. 3 Example of a plate with $[\langle 0, 45\rangle]$ stacking sequence with a complete gap (left) and complete overlap (right) implementing the edge tangency and center tangency steering strategy, respectively. The reference centerline fiber path is shown in green, while the left branch of the course is represented in blue and the right branch in red. Moreover, the gap areas are highlighted in yellow, and the overlap regions in green

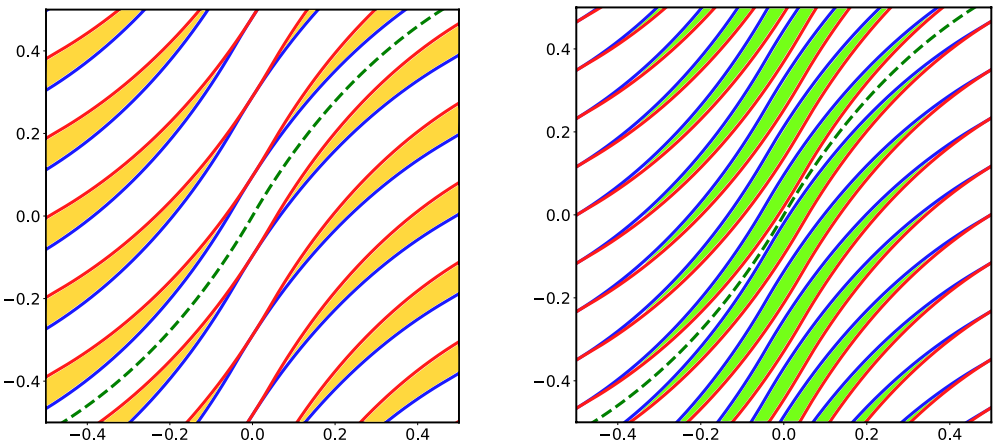

(a) $[\langle 60, 30\rangle]$ with complete gap **(b)** $[\langle 60, 30\rangle]$ with complete overlap

Fig. 4 Example of a plate with $[\langle 60, 30\rangle]$ stacking sequence with a complete gap (left) and complete overlap (right) implementing the center tangency and edge tangency steering strategy, respectively. The reference centerline fiber path is shown in green, while the left branch of the course is represented in blue and the right branch in red. Moreover, the gap areas are highlighted in yellow, and the overlap regions in green

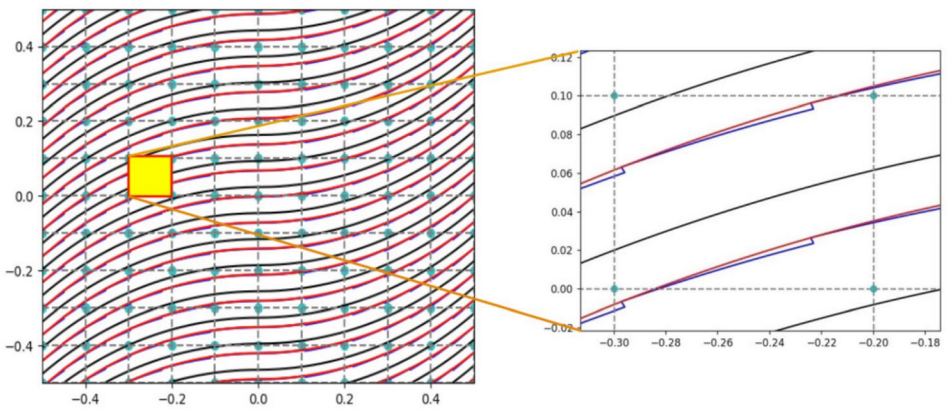

Fig. 5 Representation of the gap defect correction strategy over a $[\langle 0, 45\rangle]$ ply. The zoomed area shows the triangular gaps generated along the fiber's direction

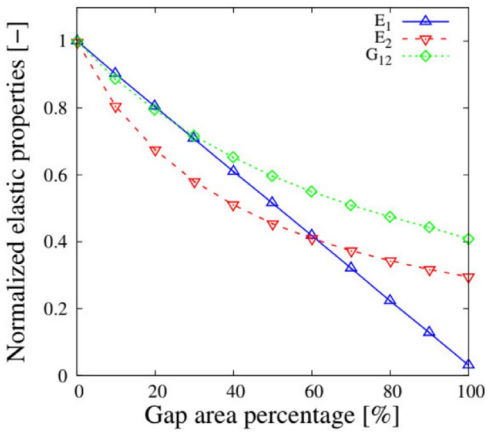

Fig. 6 Normalized elastic properties with respect to the gap area percentage. Adapted from Fayazbakhsh et al. (2013) with permission from Elsevier

100% coverage, only overlaps will be generated. Although this work investigates complete gap and complete overlap cases separately, it is worth noting that both defects can coexist within the same lamina. This typically occurs when tows are added or dropped at different stages along the fiber path, leading to mixed triangular gaps and overlap regions. Such situations are naturally described by intermediate values of the coverage parameter, i.e., between 0% and 100%, which result in a combination of the two effects. As shown in the next section, the proposed defect modeling approach is compatible with this condition, as it allows assigning local variations of thickness and material proprieties based on the spatial distribution of defects within each layer.

2.2 Defect layer method

Following the quantification and mapping of the manufacturing defects, it is essential to incorporate them into the structural model via the DLM. The incorporation of defects is accomplished by discretizing the plate's midplane and modifying the properties of the individual FE depending on the calculated percentage of defects within each FE. In this regard, the only parameter that needs to be changed to simulate the presence of flaws are the material elastic properties or the local thickness. Figure 6 shows the variation of the material elastic properties as a function of the gap area, A_{gap} within the FE, as observed by Fayazbakhsh et al. (2013). The material density varies according to the following rule of mixtures:

$$\rho_{\text{element}} = (1 - A_{\text{gap}})\rho_{\text{pre-preg}} + A_{\text{gap}}\rho_{\text{resin}} \tag{8}$$

in which $\rho_{\text{pre-preg}}$ and ρ_{resin} are the densities of the pre-impregnated tape and the resin, respectively. In the case of overlaps, the mechanical characteristics of the material are preserved, but the thickness of the FE is locally increased in proportion to the amount of overlap defect, A_{overlap}. As stated by Vijayachandran et al. (2020), due to the autoclave compaction pressure, the ply's maximum thickness increase for this research is limited to 95% as follows:

$$t_{\text{overlap}} = 0.95 t_0 (1 + A_{\text{overlap}}). \tag{9}$$

It can be summarized that when employing DLM for modeling gaps, a multimaterial plate model is generated. In this model, the thickness of each ply is maintained at a constant value and corresponds to that of the defect-free laminate. This enables the straightforward development of LW models through the modification of the material properties of each FE in both the in-plane and thickness directions. In contrast, when modeling overlaps with DLM, the thickness of each FE and layer is not constant but varies spatially. Currently, new methodologies are being explored to develop full LW plates that account for overlaps. Nevertheless, within the context of this research, high-order ESL models are preferable for modeling this particular type of defect. In the case of ESL models, the integration domain along the thickness varies for each FE. Generating an LW model with overlaps represents a complex task because of the required stair-like through-the-thickness discretization. Furthermore, modeling overlaps in an LW framework leads to a notable increase in the degrees of freedom (DOF), which may not provide additional benefits in predicting global structural responses, such as fundamental frequency and buckling load, which are the focus during the presented optimization problems.

3 Structural modeling

This paper implements the CUF framework within 2D FE. According to Carrera et al. (2014), the 3D field of displacements $\mathbf{u}^T(x, y, z) = (u, v, w)$ can be expressed as arbitrary through-the-thickness functions $F_\tau(z)$ of the generalized displacements $\mathbf{u}_\tau(x, y)$ laying in the $x - y$ plane. This reads as follows:

$$\mathbf{u}(x, y, z) = F_\tau(z)\mathbf{u}_\tau(x, y) \quad \tau = 1, \ldots, M \tag{10}$$

being M the number of expansion terms. This manuscript employs Taylor expansion (TE) and Lagrange expansion (LE) to generate ESL and LW models, respectively.

TE functions are hierarchical polynomials in the thickness coordinate z. In this approach, the displacement field is expressed as a polynomial expansion in z, ensuring a global

representation of the through-the-thickness kinematics. A second-order Taylor model is given by

$$\begin{cases} u(x,y,z) = u_0(x,y) + u_1(x,y)\cdot z + u_2(x,y)\cdot z^2 \\ v(x,y,z) = v_0(x,y) + v_1(x,y)\cdot z + v_2(x,y)\cdot z^2 \\ w(x,y,z) = w_0(x,y) + w_1(x,y)\cdot z + w_2(x,y)\cdot z^2 \end{cases} \tag{11}$$

LE functions represent an alternative approach to defining through-the-thickness displacement approximations, particularly in high-order kinematic theories. Unlike Taylor expansions, which use a global polynomial representation, LE discretize the thickness by introducing interpolation points at specific locations. This leads to a subdivision of the thickness into multiple local expansion domains, where the displacement field is approximated using Lagrange polynomials. The polynomial order is determined by the chosen set of interpolation functions. To illustrate this concept, a third-order expansion is provided in Eq. (12):

$$\begin{cases} u(x,y,z) = u_1(x,y)\,F_1(z) + u_2(x,y)\,F_2(z) + u_3(x,y)\,F_3(z) + u_4(x,y)\,F_4(z), \\ v(x,y,z) = v_1(x,y)\,F_1(z) + v_2(x,y)\,F_2(z) + v_3(x,y)\,F_3(z) + v_4(x,y)\,F_4(z), \\ w(x,y,z) = w_1(x,y)\,F_1(z) + w_2(x,y)\,F_2(z) + w_3(x,y)\,F_3(z) + w_4(x,y)\,F_4(z), \end{cases} \tag{12}$$

Usually, to describe the Lagrange functions, it is preferred to use a natural reference system where the variable ξ is defined between -1 and $+1$. Equation (13) reports the Lagrange functions related to the third-order expansion:

$$\begin{cases} F_1(z) = -\frac{9}{16}\left(\xi+\frac{1}{3}\right)\left(\xi-\frac{1}{3}\right)(\xi-1), & \xi_1 = -1, \\ F_2(z) = \frac{27}{16}(\xi-1)\left(\xi-\frac{1}{3}\right)(\xi+1), & \xi_2 = -\frac{1}{3}, \\ F_3(z) = -\frac{27}{16}(\xi+1)\left(\xi+\frac{1}{3}\right)(\xi-1), & \xi_3 = \frac{1}{3}, \\ F_4(z) = \frac{9}{16}\left(\xi+\frac{1}{3}\right)(\xi-1)\left(\xi-\frac{1}{3}\right), & \xi_4 = 1. \end{cases} \tag{13}$$

The choice between TE and LE models depends on the required accuracy and computational efficiency, as TE models provide a global polynomial approximation while LE models allow localized high-order variations in the displacement field. The continuity of the displacements at the layer interfaces is imposed to obtain a Lagrange displacement-based (LD) LW approach, as prescribed in Carrera (2002). In this context, TE*n* and LD*n* denote the use of Taylor and Lagrange polynomials of the *n*th order, respectively. In addition, *X*LD*n* is used for LW models to indicate the use of *X* Lagrange polynomials of *n*th order per layer. Subsequently, coupling CUF with the FE method, the 3D displacement field is expressed as follows:

$$\mathbf{u}(x,y,z) = N_i(x,y)F_\tau(z)\mathbf{q}_{\tau i} \quad i = 1,\dots,N_n \quad \tau = 1,\dots,M \tag{14}$$

where N_n is the number of nodes in the FE, and $\mathbf{q}_{\tau i}$ is the unknowns vector. The present work utilizes bi-quadratic FEs, referred to as Q9, as the $N_i(x,y)$ shape functions.

The governing equations are derived from the principle of virtual displacements (PVD). The problem is described in terms of virtual work using the principle underlying PVD, which, in the case of free vibration analysis, can be expressed as follows:

$$\delta\mathcal{L}_{\text{int}} + \delta\mathcal{L}_{\text{ine}} = 0 \tag{15}$$

where the virtual variation of the internal work, $\delta\mathcal{L}_{\text{int}}$, and the virtual variation of the inertial work, $\delta\mathcal{L}_{\text{ine}}$, read as

$$\delta\mathcal{L}_{\text{int}} = \int_V \delta\boldsymbol{\epsilon}^T\boldsymbol{\sigma}\,\mathrm{d}V \tag{16}$$

$$\delta\mathcal{L}_{\text{ine}} = \int_V \delta\mathbf{u}^T\rho\ddot{\mathbf{u}}\,\mathrm{d}V \tag{17}$$

Equation (16) can be reformulated by employing Eq. (14), the geometrical relations between strains and displacements and the constitutive relations between stresses and strains, resulting in

$$\delta\mathcal{L}_{\text{int}} = \delta\mathbf{q}_{sj}^T\left[\int_V \mathbf{D}^T(N_jF_s)\widetilde{\mathbf{C}}\mathbf{D}(N_iF_\tau)\mathrm{d}V\right]\mathbf{q}_{\tau i} = \delta\mathbf{q}_{sj}^T\mathbf{k}^{ij\tau s}\mathbf{q}_{\tau i} \tag{18}$$

where $\mathbf{k}^{ij\tau s}$ is the 3×3 fundamental nucleus (FN) of the stiffness matrix of the single layer, which is an invariant of the order of the $N_i(x,y)$ shape function and the $F_\tau(z)$ theory expansion. Further insight on the FN assembly of ESL and LW models is available later in this section. $\mathbf{D}(\cdot)$ is the differential operator containing the geometrical relations between strains and displacements, and $\widetilde{\mathbf{C}}$ is the material stiffness matrix defined in the global reference frame. Since this work considers varying fiber paths within the $x-y$ plane, $\widetilde{\mathbf{C}}$ is evaluated point-wise as $\widetilde{\mathbf{C}} = \mathbf{T}(x,y)\mathbf{C}\mathbf{T}^T(x,y)$, being $\mathbf{C}$ the matrix containing the elastic coefficients of orthotropic material, and $\mathbf{T}$ is the rotation matrix, as explained in Reddy (2004). Unlike conventional codes, where the fiber orientation is typically assumed constant within each FE, the present implementation evaluates the spatially varying stiffness tensor $\widetilde{\mathbf{C}}$ at the Gauss integration points. This strategy ensures a more accurate representation of the local

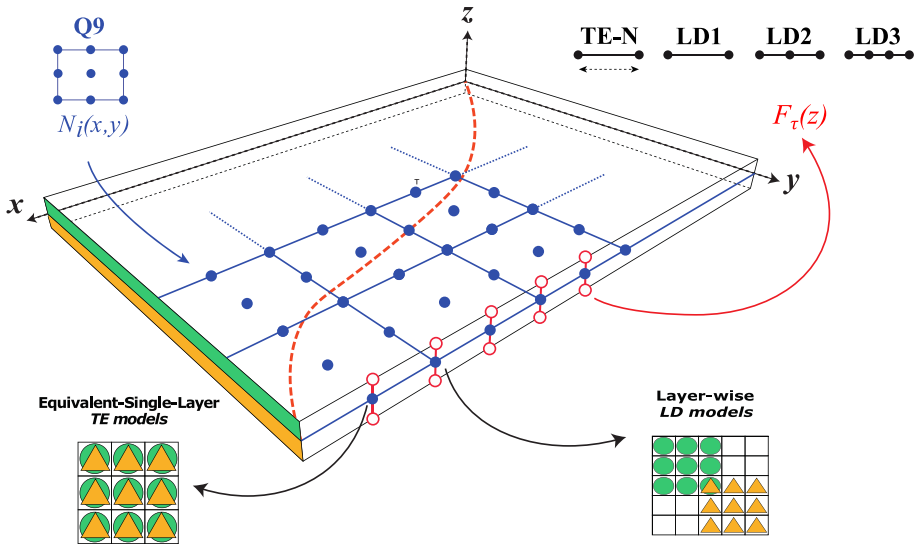

Fig. 7 Procedures for assembling ESL and LW plate models

anisotropic behavior induced by tow steering. In addition, the number of Gauss points can be increased independently of the FE interpolation order, improving integration accuracy without increasing the total number of degrees of freedom. As a result, accurate simulations of VAT laminates can be obtained without resorting to extremely fine meshes since the desired accuracy is achieved by increasing the order of the through-the-thickness expansion functions. A similar approach is applied to Eq. (17), yielding

$$\delta\mathcal{L}_{\text{ine}} = \delta\mathbf{q}_{sj}^{T}\left[\int_{V}\rho\mathbf{I}F_{\tau}F_{s}N_{i}N_{j}\mathrm{d}V\right]\ddot{\mathbf{q}}_{\tau i} = \delta\mathbf{q}_{sj}^{T}\mathbf{m}^{ij\tau s}\ddot{\mathbf{q}}_{\tau i} \tag{19}$$

in which $\mathbf{I}$ denotes the 3×3 identity matrix and $\mathbf{m}^{ij\tau s}$ is the 3×3 diagonal FN of the mass matrix, as explained in Carrera et al. (2014). The structure's global mass and stiffness matrices are obtained from their respective FNs based on the shape and expansion functions. These matrices are assembled by looping over the τ and s expansion indices and the i and j FE indices. Thus, the undamped free vibration problem can be expressed as follows:

$$\mathbf{M}\ddot{\mathbf{q}} + \mathbf{K}\mathbf{q} = 0 \tag{20}$$

where $\mathbf{M}$ and $\mathbf{K}$ represent the global mass and stiffness matrices, respectively. The assembly of the stiffness matrix, $\mathbf{K}$, depends on the selected modeling approach. The ESL and LW models are frequently employed strategies for analyzing multilayered structures. In the context of ESL modeling, the properties of each layer are homogenized and subsequently combined to compute the stiffness matrix. However, as observed in Carrera (1997), ESL does not satisfy the C_z^0 continuity requirements. In contrast, the LW modeling approach assumes that each layer is treated independently, expanding the displacement field within each lamina. Consequently, displacement continuity must be enforced at each interface (Carrera 2002), ensuring the C_z^0 requirements are satisfied. The two assembly approaches are illustrated in Fig. 7 for a plate with two layers.

Assuming a pure harmonic solution $\mathbf{q} = \widetilde{\mathbf{q}}e^{i\omega t}$, Eq. (20) results in the following eigenvalue problem:

$$\left(\mathbf{K} - \omega_i^2\mathbf{M}\right)\widetilde{\mathbf{q}}_i = 0 \tag{21}$$

in which ω_i is the ith natural frequency and $\widetilde{\mathbf{q}}_i$ represents the ith eigenvector.

The buckling study consists of solving the equation:

$$|\mathbf{K}_T| = 0 \tag{22}$$

where $\mathbf{K}_T$ is the tangent stiffness matrix of the structure. The expression for this matrix is retrieved by linearizing the virtual variation of the internal strain energy:

$$\delta^2(\mathcal{L}_{\text{int}}) = \int_V \delta\left(\delta\boldsymbol{\epsilon}^T\boldsymbol{\sigma}\right)\mathrm{d}V = \int_V \left[\delta\left(\delta\boldsymbol{\epsilon}^T\right)\boldsymbol{\sigma} + \delta\boldsymbol{\epsilon}^T\delta\boldsymbol{\sigma}\right]\mathrm{d}V \tag{23}$$

Substituting Eq. (14), the constitutive law, and the geometrical relations between strains and displacements, the previous equation is rewritten for the case of linearized buckling as follows:

$$\delta^2(\mathcal{L}_{\text{int}}) = \delta\mathbf{q}_{sj}^{T}\mathbf{k}_{T}^{ij\tau s}\delta\mathbf{q}_{\tau i} \approx \delta\mathbf{q}_{sj}^{T}\left(\mathbf{k}^{ij\tau s} + \mathbf{k}_{\sigma}^{ij\tau s}\right)\delta\mathbf{q}_{\tau i} \tag{24}$$

where $\mathbf{k}_{\sigma}^{ij\tau s}$ denotes the 3×3 FN of the geometric stiffness matrix. This work does not include the explicit equations that allow calculating the tangent stiffness matrix but can be found in Wu et al. (2019). The linearized buckling analysis is performed under the following assumptions: (i) the pre-buckling equilibrium state is stable; (ii) the initial stress remains constant and varies neither in magnitude nor in direction during buckling; (iii) at the bifurcation,

the equilibrium states are infinitesimally adjacent so that linearization is possible. At the bifurcation, there exists a critical value λ_{cr} of the load factor for which an equilibrium configuration exists where:

$$|\mathbf{K} + \lambda_{cr}\mathbf{K}_\sigma| = 0. \tag{25}$$

In this regard, the buckling load can be computed as $P_{cr} = \lambda_{cr}P_0$, where P_0 is the applied load. In Eq. (25), $\mathbf{K}_\sigma$ denotes the assembled geometric stiffness matrix of the structure, obtained by looping over the τ, s, i, and j indices of $\mathbf{k}_\sigma^{ij\tau s}$.

4 Optimization framework

Since the definition of the fiber path of a single ply in a tow-steered composite involves multiple continuous parameters (see Eq. (1)), VAT composites inherently span a much larger, essentially infinite, design space compared to traditional straight-fiber composite laminates. Thus, the design space needs to be explored efficiently to exploit all the possibilities that this kind of structure offers. Besides, if the quantities of interest that aim to be tailored are, a priori, discontinuous, an effective optimization technique must be considered.

This manuscript aims to simultaneously minimize the mass of a VAT plate and maximize a second quantity of interest (QoI), viz., the fundamental frequency or the buckling load. The former depends on the number of plies comprising the laminate, while the latter depends on the fiber path design parameters for a fixed number of layers. Unlike continuous topology optimization frameworks, which optimize material distribution and thickness fields across the design domain (Urso et al. 2023; Urso and Montemurro 2024; Montemurro et al. 2024); this study adopts a discrete approach where the number of plies is treated as an integer-valued parameter while the fiber path parameters remain continuous. Therefore, a mixed-integer, multi-objective optimization problem is faced. In the case that no manufacturing limitations are considered, the optimization problem is stated as follows:

$$\begin{aligned}
\min_{\mathbf{x}} \quad & [\text{mass}(\mathbf{x}),\ -\text{QoI}(\mathbf{x})] \\
\text{w.r.t.} \quad & \mathbf{x} = \left(N_{\text{ply}}, \mathbf{T}_0, \mathbf{T}_1\right), \\
\text{subject to} \quad & N_{\text{ply}} \in \{N_{\text{ply}}^L, \dots, N_{\text{ply}}^U\}, \\
& \mathbf{T}_0 \in [-90°, 90°]^{N_{\text{ply}}}, \\
& \mathbf{T}_1 \in [-90°, 90°]^{N_{\text{ply}}}.
\end{aligned} \tag{26}$$

in which N_{ply} is the number of layers for each design, varying between the lower N_{ply}^L and upper N_{ply}^U bound, and $\mathbf{T}_0$ and $\mathbf{T}_1$ are the vectors containing the individual T_0 and T_1 angles for each layer of the current design. To reduce the number of design variables and ensure practical stacking sequences, symmetry, and quasi-symmetry were enforced a priori. Symmetric laminates were used when N_{ply} is even, while quasi-symmetric configurations were adopted for odd-layered designs.

The solutions to the unconstrained multi-objective could not be feasible from a manufacturing perspective. Therefore, manufacturing limitations must be considered. As anticipated in Sect. 2, the main constraint considered is the AFP head's turning radius. This is a constraint that needs to be fulfilled for each layer in the laminate. In this context, the constrained multi-objective optimization problem can be posed as follows:

$$\begin{aligned}
\min_{\mathbf{x}} \quad & [\text{mass}(\mathbf{x}),\ -\text{QoI}(\mathbf{x})] \\
\text{w.r.t.} \quad & \mathbf{x} = \left(N_{\text{ply}}, \mathbf{T}_0, \mathbf{T}_1\right), \\
\text{subject to} \quad & N_{\text{ply}} \in \{N_{\text{ply}}^L, \dots, N_{\text{ply}}^U\}, \\
& \mathbf{T}_0 \in [-90°, 90°]^{N_{\text{ply}}}, \\
& \mathbf{T}_1 \in [-90°, 90°]^{N_{\text{ply}}}, \\
& \prod_{i=1}^{N_{\text{ply}}} \max\left(1, \frac{\kappa_{\max}^{(i)}}{\kappa_{\lim}}\right) = 1.
\end{aligned} \tag{27}$$

where the manufacturing constraint is aggregated through a product of a maximum value operator over the number of layers in the design. The max(·) operator chooses between 1 and the ratio $\kappa_{\max}^i/\kappa_{\lim}$. In this regard, if the curvature constraint is satisfied for all the plies, the product will equal 1. This formulation ensures that if a single layer exceeds the permissible curvature, the collective constraint will be violated, thereby steering the optimizer away from inherently infeasible designs. Using the product operator, the optimization solver can identify how far the evaluated design is from fulfilling the manufacturing constraint for all the plies in the design.

In this study, the non-dominated sorting genetic algorithm II (NSGA-II) (Deb 2001), incorporated in modeFrontier©(Nardin et al. 2009), is employed to address the mixed-integer, multi-objective optimization problem associated with VAT laminates. NSGA-II is particularly well-suited for this application due to its robustness in handling complex design spaces that combine discrete and continuous variables (Jaber et al. 2021), as required here to simultaneously optimize the number of laminate plies and fiber orientation angles. Unlike traditional gradient-based optimization methods, NSGA-II does not require derivative information, making it highly effective for the inherently discontinuous, multi-modal design space of VAT laminates (Montemurro and Catapano 2016). The algorithm's non-dominated sorting and crowding distance mechanisms are crucial for identifying a diverse set of optimal solutions across the Pareto front, balancing mass minimization

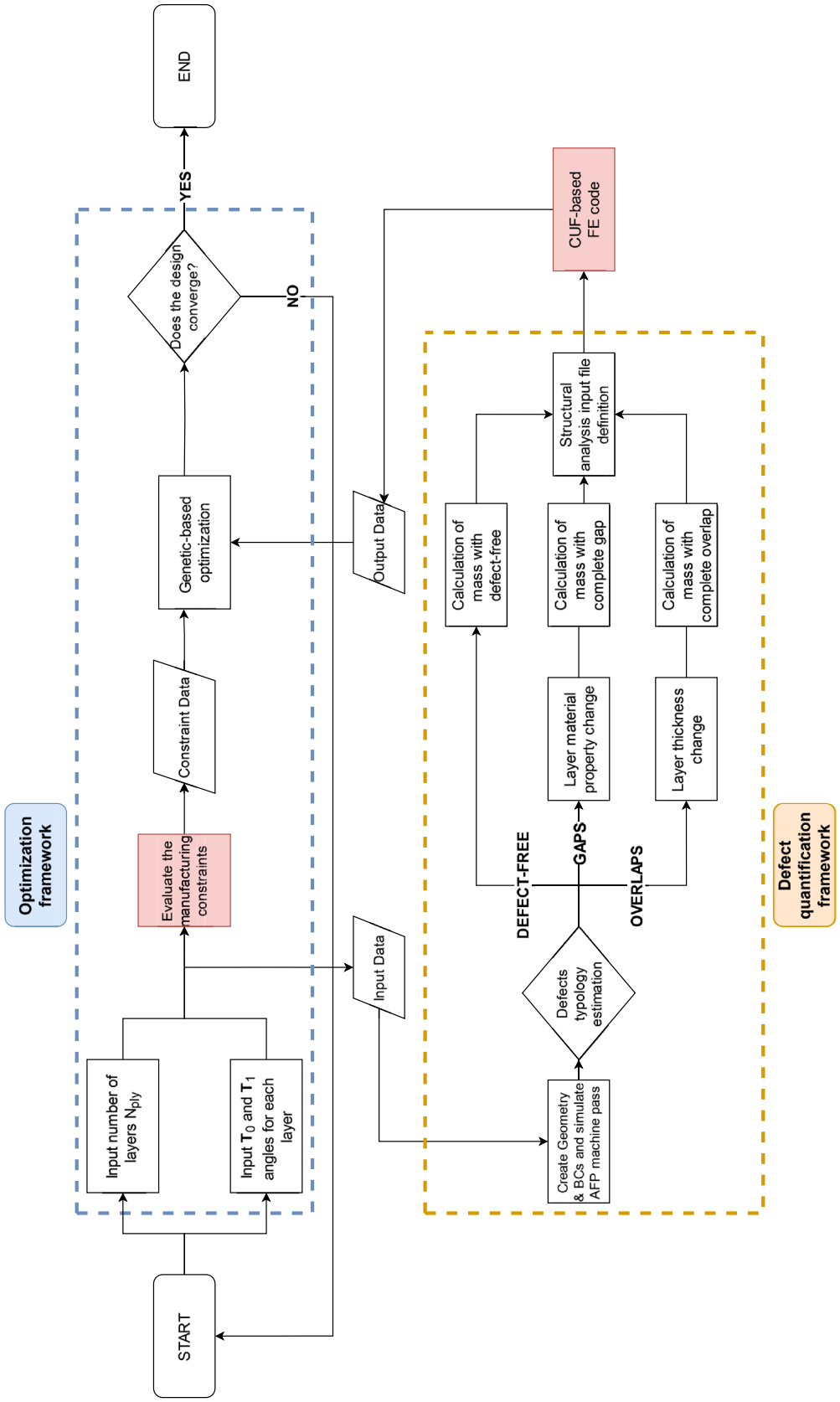

Fig. 8 Flowchart of the multi-objective mixed-integer optimization framework considering the manufacturing constraint $\kappa_{\text{lim}} = 3.28\ \text{m}^{-1}$ and the quantification of the defects performed by DLM. Finally, the CUF-based FE code is used to calculate the fundamental frequency and buckling load

Table 2 Material properties of the pre-impregnated tows and resin used in Akbarzadeh et al. (2014)

	E_1 [GPa]	$E_2 = E_3$ [GPa]	G_{12} [GPa]	$G_{13} = G_{23}$ [GPa]	ν_{12} [–]	ρ [kg/m^3]
Tow	143	9.1	4.82	4.9	0.3	1500
Resin	3.72	3.72	1.43	1.43	0.3	1100

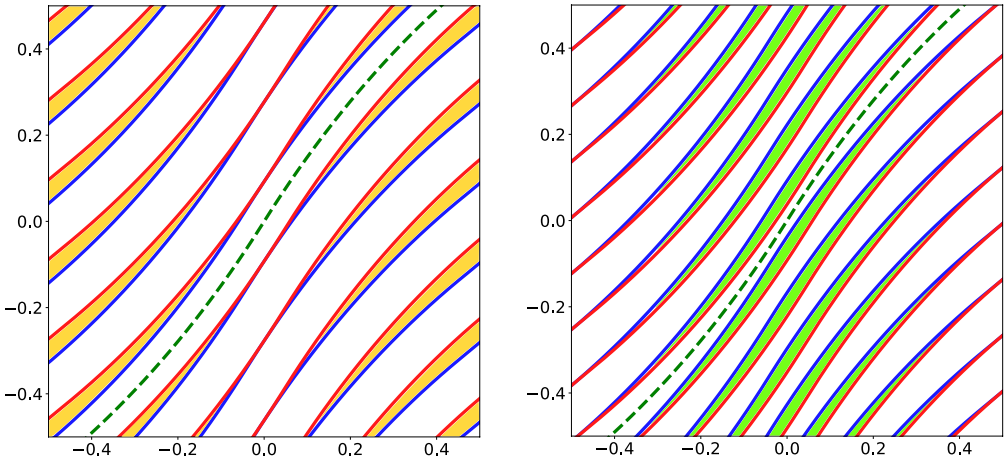

(a) $[\langle 58, 39\rangle]$ with complete gap (b) $[\langle 58, 39\rangle]$ with complete overlap

Fig. 9 Reference plate from Akbarzadeh et al. (2014) with $[\langle 58, 39\rangle]$ stacking sequence with a complete gap (left) and complete overlap (right) implementing the center tangency and edge tangency steering strategy, respectively

with performance maximization (regarding fundamental frequency and buckling load). Moreover, NSGA-II's elitist approach ensures that the best solutions in each generation are retained, accelerating convergence towards the Pareto-optimal front. This feature is vital for optimization problems like the one in this study, where manufacturing constraints such as the AFP head turning radius impose strict limits on feasible fiber paths. These enhancements, implemented within the NSGA-II framework, are particularly suited to addressing the complexities of mixed-integer optimization in VSC design. They enable efficient exploration of the high-dimensional design space while ensuring computational feasibility, as demonstrated by Jaber et al. (2021). Utilizing the product-based aggregation form of the optimization constraint, as seen in Eq. (27), within the NSGA-II framework guides the algorithm away from infeasible designs by evaluating curvature compliance collectively across all layers, rather than filtering each layer individually. This approach allows NSGA-II to focus effectively on feasible regions of the design space.

A key aspect of this optimization strategy is the synergy between NSGA-II and the DLM, explained in Sect. 2, which is incorporated to quantify manufacturing defects in the numerical model. The DLM operates in conjunction with NSGA-II, providing accurate defect quantification for each evaluated design, which is crucial for a realistic assessment of VAT performance. Figure 8 illustrates the

Table 3 Effect of the structural theory on the first fundamental frequency for the complete gap and overlap manufacturing strategies

Complete gap			Complete overlap		
Model	DOFs	f_1 [Hz]	Model	DOFs	f_1 [Hz]
Akbarzadeh et al. (2014)	–	30.95	Akbarzadeh et al. (2014)	–	36.19
ESL-TE 1	1041	32.17	ESL-TE 1	1041	37.00
ESL-TE 2	1521	31.91	ESL-TE 2	1521	36.65
ESL-TE 3	2028	31.90	ESL-TE 3	2028	36.64
LW-1LD1	8619	31.89	ESL-TE 4	2535	36.64
LW-1LD2	16,731	31.89	ESL-TE 5	3042	36.64

Each model uses a $6 \times 6Q9$ FE mesh

optimization workflow of the constrained problem. In the case of the unconstrained optimization, the check on the manufacturing constraint is skipped. First, an initial set of individuals is generated, whose design variables are the number of layers in the laminate and the fiber path angles. Subsequently, based on the different T_0 and T_1, the maximum curvature of the fiber path is calculated. Then, the input data of the FE analysis is generated. Only the number of expansion domains and the fiber angle orientation are modified if the defect-free condition is considered. Otherwise, if a complete gap or overlap condition is preferred, the material and thickness of each FE are modified

according to the DLM. In addition, depending on the fabrication strategy, the mass of the plate is calculated as

$$\begin{aligned} m_{\text{gap}} &= \sum_{i=1}^{N_{\text{ply}} \cdot N_{\text{FE}}} \rho_i \cdot a^2 t_0 = a^2 t_0 \sum_{i=1}^{N_{\text{ply}} \cdot N_{\text{FE}}} \rho_i \\ m_{\text{overlap}} &= \sum_{i=1}^{N_{\text{ply}} \cdot N_{\text{FE}}} \rho_{\text{elem}} a^2 \cdot t_i = a^2 \rho_{\text{elem}} \sum_{i=1}^{N_{\text{ply}} \cdot N_{\text{FE}}} t_i \end{aligned} \tag{28}$$

where ρ_i is the homogenized density associated with the gap-defective FE, which is computed through the rule of mixtures, t_i is the thickness associated with the overlap-defective FE, calculated according to Eq. (9), and N_{FE} is the number of FE in the numerical model. Then, the FE simulation is launched, and the value of the fundamental frequency or buckling load is retrieved. Last, the genetic operations are performed until convergence of the Pareto front is reached.

5 Numerical results

5.1 Defect modeling verification

The defect-mapping procedure depicted in Sect. 2 is verified against the results present in the work by Akbarzadeh et al. (2014) for fundamental frequency and buckling load. The structure under investigation is a 16-layered symmetric and balanced $[\pm\langle 58, 39\rangle]_{4s}$ laminate and width-to-thickness ratio $a/h = 200$. The width and length of the plate are $a = b = 1$ m, and the individual ply thickness equals 0.159 mm. The plate is simply supported on all four sides. The mechanical properties of the pre-impregnated tows and the resin are listed in Table 2. The reference plate is illustrated in Fig. 9. In particular, Fig. 9a depicts gaps at the edges, while Fig. 9b illustrates the presence of overlaps in the central area.

The effect of the structural theory is addressed in the presence of manufacturing signature after performing a convergence analysis on the number of FE. In the case of fundamental frequency verification, a $6 \times 6Q9$ mesh is employed because of the trade-off between accuracy and computational time. Gap-defective plates are modeled through ESL and LW models. In contrast, overlap-defective plates are modeled only with ESL models due to the high computational cost of modeling overlaps with an LW approach, as explained in Sect. 2. Table 3 shows the first fundamental frequency results for the complete gap and complete overlap strategies. Although there is a good agreement between the proposed methodology and the reference solution, there exist slight differences. The reasons are twofold: (i) the reference solution employs Reddy (2004) third-order shear deformation theory, which assumes a constant u_z displacement component while the present method foresees high-order terms for the three displacement components; and (ii) the reference values are obtained through a semi-analytical approach employing the Galerkin method and Fourier series expansion to solve the governing differential equations, whereas the present work employs a fully numerical method. In addition, it is found that, in the case of complete gap strategy, there is no significant difference between ESL and LW models in terms of the predicted f_1. In the case of complete overlap, there is no meaningful difference as the order of TE increases.

The defect-mapping procedure is then verified to predict the buckling load of VAT plates in the presence of defects. The laminated structure described above is now subject to an in-plane shortening at $x = \pm a/2$. The dimensionless buckling loads $\tilde{N} = N_{\text{cr}} a^2 / E_2 h^3$ predicted by the various structural theories are displayed in Table 4. A $10 \times 10Q9$ mesh is utilized because of the accuracy and computational time trade-off. A good correlation is found between the present results and the reference, with the differences lower than the first fundamental frequency case. The reasons for the discrepancies have been mentioned above, i.e., the reference's structural theory and solution approach. Regarding the present structural models, ESL

Table 4 Effect of the structural theory on the dimensionless buckling load for the complete gap and overlap manufacturing strategies

Complete gap			Complete overlap		
Model	DOFs	$\tilde{N}$ [–]	Model	DOFs	$\tilde{N}$ [–]
Akbarzadeh et al. (2014)	–	24.47	Akbarzadeh et al. (2014)	–	37.44
ESL-TE 1	2646	25.07	ESL-TE 1	2646	37.86
ESL-TE 2	3969	24.64	ESL-TE 2	3969	37.16
ESL-TE 3	5292	24.61	ESL-TE 3	5292	37.11
LW-1LD1	22,491	24.60	ESL-TE 4	6615	37.11
LW-1LD2	43659	24.60	ESL-TE 5	7938	37.10

Each model uses a $10 \times 10Q9$ FE mesh

Table 5 Material properties of the pre-impregnated tows and resin used for the mass versus fundamental frequency optimization

	E_1 [GPa]	$E_2 = E_3$ [GPa]	G_{12} [GPa]	$G_{13} = G_{23}$ [GPa]	ν_{12} [–]	ρ [kg/m^3]
Tow	143	9.10	4.82	4.90	0.30	1650
Resin	3.70	3.70	1.40	1.40	0.30	1310

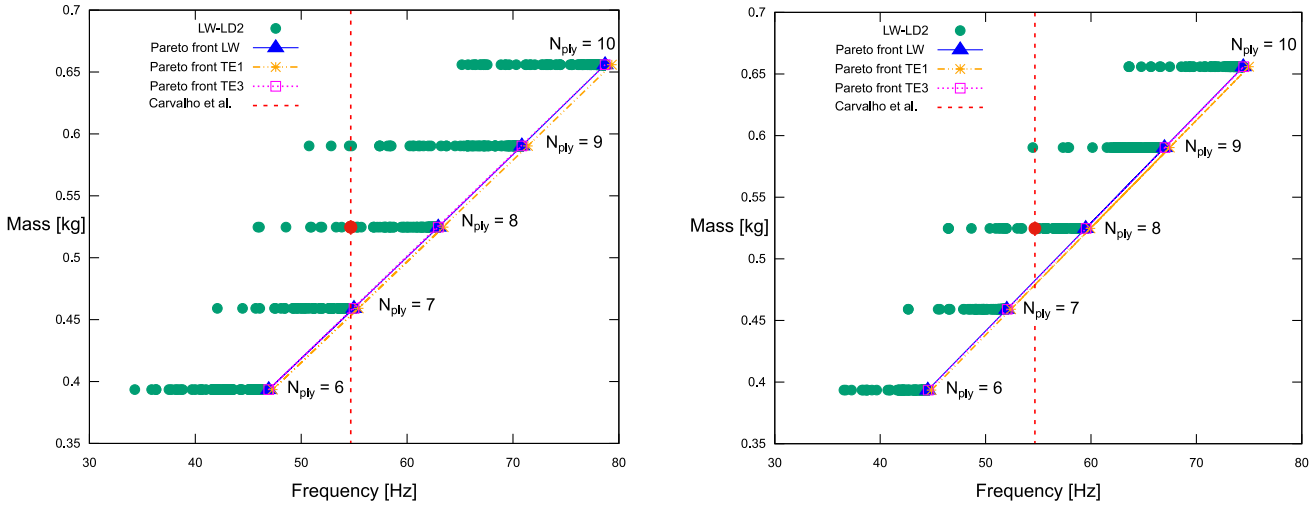

(a) Unconstrained Pareto front (b) Constrained Pareto front

Fig. 10 Defect-free Pareto fronts for the mass versus fundamental frequency optimization, illustrating the (**a**) unconstrained and (**b**) constrained cases. The results are derived using ESL and LW models to reflect the influence of different structural theories

Table 6 Design results for the defect-free unconstrained and constrained problems

	Unconstrained			Constrained		
	ESL-TE1	ESL-TE3	LW-LD2	ESL-TE1	ESL-TE3	LW-LD2
$\langle T_0, T_1 \rangle^1$ [°]	$\langle -90, 6 \rangle$	$\langle -90, 7 \rangle$	$\langle -90, 6 \rangle$	$\langle -86, -31 \rangle$	$\langle -85, -30 \rangle$	$\langle -85, -30 \rangle$
$\langle T_0, T_1 \rangle^2$ [°]	$\langle 90, -9 \rangle$	$\langle 90, -9 \rangle$	$\langle 90, -9 \rangle$	$\langle 79, 26 \rangle$	$\langle 72, 22 \rangle$	$\langle 76, 25 \rangle$
$\langle T_0, T_1 \rangle^3$ [°]	$\langle 90, -9 \rangle$	$\langle 90, -8 \rangle$	$\langle 90, -8 \rangle$	$\langle -60, -12 \rangle$	$\langle -61, -13 \rangle$	$\langle -61, -13 \rangle$
$\langle T_0, T_1 \rangle^4$ [°]	$\langle -90, 6 \rangle$	$\langle -90, 8 \rangle$	$\langle -90, 7 \rangle$	$\langle 58, 10 \rangle$	$\langle 70, 20 \rangle$	$\langle 62, 15 \rangle$
f_1 [Hz]	$55.43^{+1.37\%}$	$54.99^{+0.57\%}$	$54.98^{+0.55\%}$	$52.42^{-4.12\%}$	$52.06^{-4.79\%}$	$52.01^{-4.87\%}$
mass [kg]	$0.4591^{-12.5\%}$	$0.4591^{-12.5\%}$	$0.4591^{-12.5\%}$	$0.4591^{-12.5\%}$	$0.4591^{-12.5\%}$	$0.4591^{-12.5\%}$

The superscripts indicate the relative differences compared to the optimal reference solution reported in Carvalho et al. (2022)

and LW theories lead to similar values of dimensionless buckling load when the complete gap strategy is chosen. In the case of complete overlap, the ESL-TE 1 model presents the largest value of $\tilde{N}$ compared to higher order ESL theories. In any case, the differences in results between the modeling strategies are minimal because of the large width-to-thickness ratio $a/h = 200$ of the plate under study. If a thicker plate were analyzed, the shear stress components would be more relevant, and higher order models would be required.

5.2 Least-weight design optimization

5.2.1 Mass versus fundamental frequency optimization

The first least-weight problem combines minimizing a laminated plate's mass and maximizing its fundamental frequency. The AFP machine's manufacturing signature and strategy are included in the optimization loop following the procedure depicted in Sect. 4. The plate under investigation has a width and length $a = b = 0.50$ m and a ply thickness of 0.159 mm and is fully clamped. The material properties are available in Table 5.

The optimization results are compared against the optimal straight-fiber case reported in Carvalho et al. (2022). This work only considered the fundamental frequency as the objective function. The number of plies was fixed to eight, and symmetry was imposed a priori for the laminate stacking sequence. The present work considers symmetric laminates to reduce the number of design variables. The optimal solution by Carvalho et al. (2022) presents a $[90°, 0°, 90°, 0°]_s$ lamination, a fundamental frequency equal to 54.68 Hz, evaluated with the FEM implemented in the present work and the $6 \times 6Q9$ mesh, and a mass of 0.5247 kg.

Figure 10b displays the Pareto fronts of the defect-free manufacturing strategy and different structural theories for

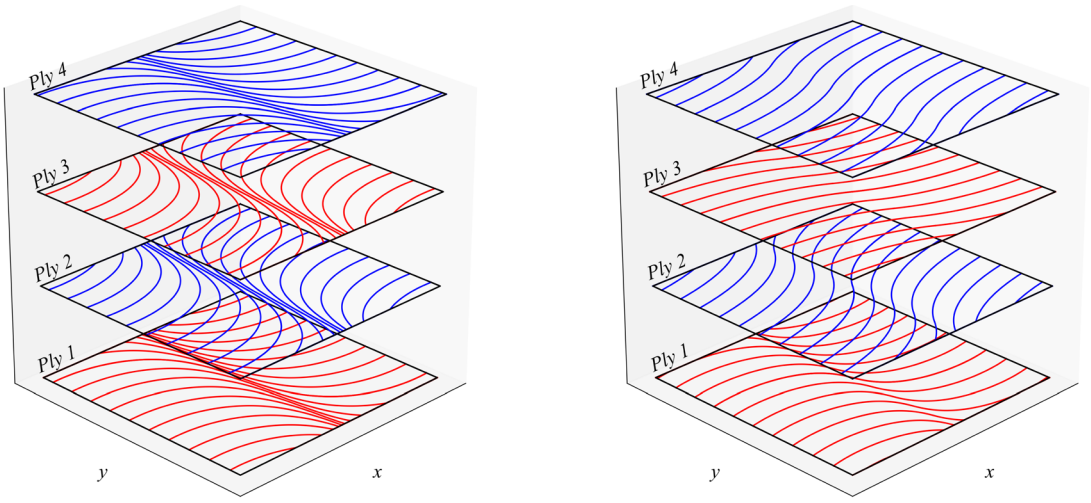

(a) Defect-free unconstrained optimal fiber path (b) Defect-free constrained optimal fiber path

Fig. 11 Defect-free unconstrained and constrained optimal fiber paths using LW-LD2 structural theory, shown for half of the laminate due to its quasi-symmetric configuration

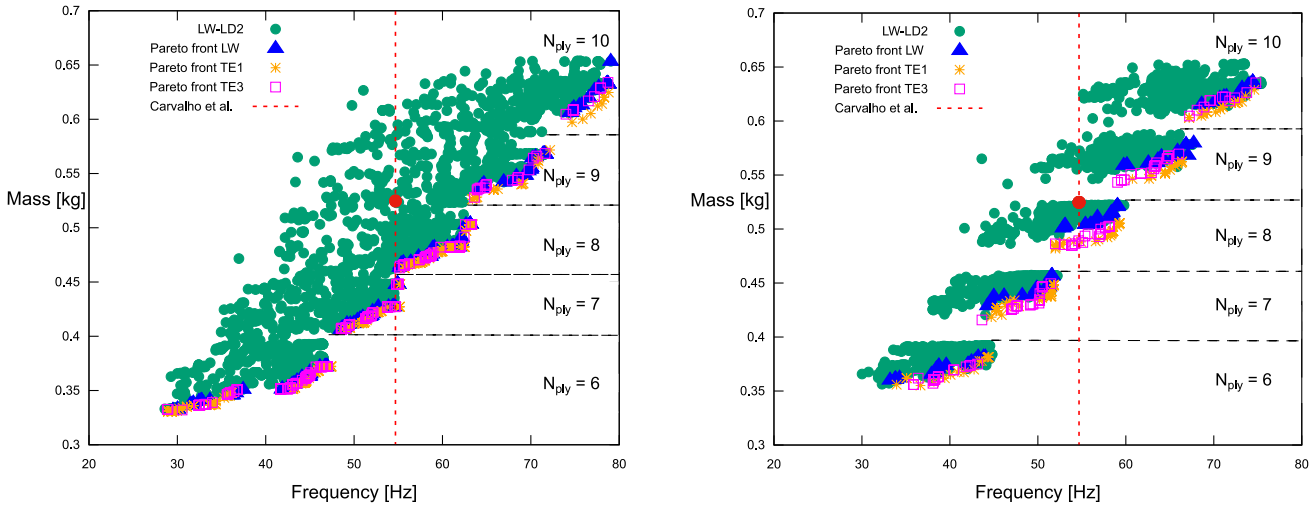

(a) Unconstrained Pareto front (b) Constrained Pareto front

Fig. 12 Complete gap Pareto fronts for the mass versus fundamental frequency optimization, illustrating the (**a**) unconstrained and (**b**) constrained cases. The results are derived using ESL and LW models to account for the influence of the structural theory

the unconstrained and manufacture-constrained problems. The optimization constraint κ_{lim} is set equal to 3.28 m^{-1}. Table 6 provides the stacking sequence for the seven-layered non-dominated design, while Fig. 11 illustrates the optimal fiber paths in the defect-free scenario utilizing the LW-LD2 structural theory for both unconstrained and constrained solutions. For the mass versus fundamental frequency optimization case, it was decided to represent the fiber paths of only half of the laminate, as the structure is symmetric. The complete gap Pareto fronts are depicted in Fig. 12, and the corresponding seven-layered designs are presented in Table 7. The optimal symmetrical fiber paths for the LW-LD2 model, determined under the specified manufacturing conditions, are illustrated in Fig. 13. Finally, the Pareto front for the complete overlap strategy is presented in Fig. 14, with the corresponding symmetrical six-layered overlap designs detailed in Table 8. The optimal fiber paths for the ESL-TE3 model under the complete overlap strategy are depicted in Fig. 15. It is worth noting that the green dots in the Pareto fronts correspond to all the designs evaluated during the optimization process utilizing

Table 7 Design results for the complete gap unconstrained and constrained problem

	Unconstrained			Constrained		
	ESL-TE1	ESL-TE3	LW-LD2	ESL-TE1	ESL-TE3	LW-LD2
$\langle T_0, T_1 \rangle^1$ [°]	$\langle -89, -7 \rangle$	$\langle -86, 5 \rangle$	$\langle -85, 0 \rangle$	$\langle 85, 30 \rangle$	$\langle 86, 31 \rangle$	$\langle 87, 32 \rangle$
$\langle T_0, T_1 \rangle^2$ [°]	$\langle -86, 6 \rangle$	$\langle 89, -7 \rangle$	$\langle 86, -8 \rangle$	$\langle -58, -12 \rangle$	$\langle -60, -12 \rangle$	$\langle -59, -12 \rangle$
$\langle T_0, T_1 \rangle^3$ [°]	$\langle 89, -10 \rangle$	$\langle 89, -4 \rangle$	$\langle 89, 2 \rangle$	$\langle 27, -12 \rangle$	$\langle 34, -10 \rangle$	$\langle 28, -7 \rangle$
$\langle T_0, T_1 \rangle^4$ [°]	$\langle 89, -16 \rangle$	$\langle 89, -5 \rangle$	$\langle 89, 8 \rangle$	$\langle 53, 88 \rangle$	$\langle 51, 88 \rangle$	$\langle 47, 87 \rangle$
f_1 [Hz]	$55.19^{+0.93\%}$	$54.67^{-0.02\%}$	$54.61^{-0.13\%}$	$52.35^{-4.26\%}$	$51.91^{-5.07\%}$	$51.84^{-5.19\%}$
mass [kg]	$0.4272^{-18.58\%}$	$0.4273^{-18.56\%}$	$0.4274^{-18.52\%}$	$0.4482^{-14.56\%}$	$0.4482^{-14.58\%}$	$0.4486^{-14.50\%}$

The superscript indicates the relative difference with respect to the optimal reference solution from Carvalho et al. (2022)

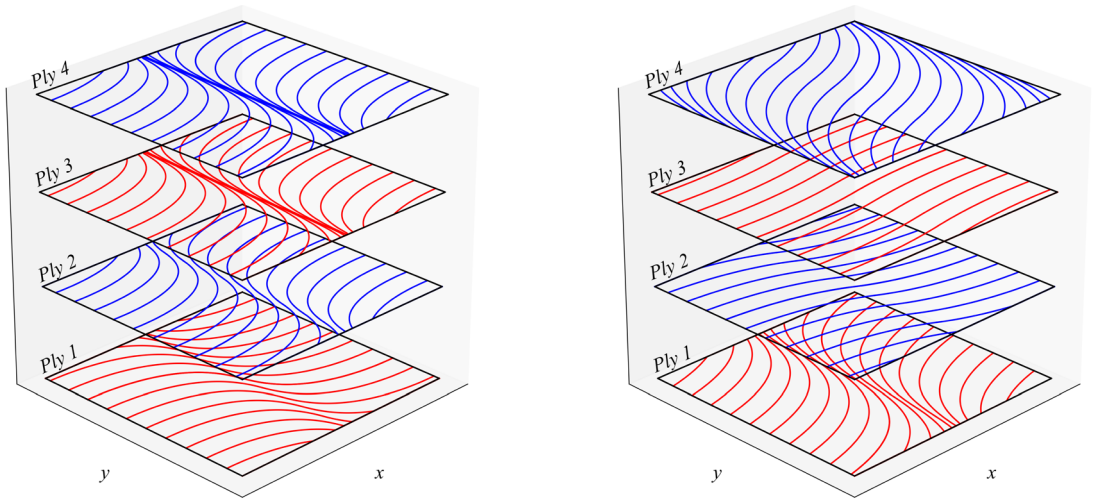

(a) Complete gap unconstrained optimal fiber path (b) Complete gap constrained optimal fiber path

Fig. 13 Complete gap unconstrained and constrained optimal fiber paths using LW-LD2 structural theory, shown for half of the laminate due to its quasi-symmetric configuration

the LW-LD2 structural model for defect-free and complete gap manufacturing strategies. In the complete overlap Pareto fronts, the green dots correspond to the ESL-TE3 designs. The designs of the low-order ESL theories are not represented for the sake of clearness.

From the results outlined, the following comments can be made:

- The discrete nature of the optimization problem is highlighted in the defect-free and complete gap manufacturing strategies. The former presents a constant mass for each ply while the fundamental frequency varies. The latter exhibits a scattered set of designs, where the mass and fundamental frequency vary, even when the number of layers is kept constant. These banded sets are better appreciated in the complete gap-constrained Pareto front in Fig. 12b, which are due to the density associated with each FE, as depicted in Eq. (28). These banded fronts do not exist in the complete overlap optimization results, in which the parameter varying the mass for a fixed number of plies is the thickness associated with each FE.
- There is a weak influence of the structural theory on the defect-free case's unconstrained and constrained Pareto fronts. This is further observed in Table 6, where the only discrepancy occurs for $\langle T_0, T_1 \rangle^4$ in the constrained case.
- A slight variability is observed in the Pareto fronts corresponding to the complete gap and overlap strategies, as shown in Figs. 12 and 14, respectively. This variation becomes more pronounced as the number of plies increases and is attributable to the different structural models employed. Despite this, the optimal fiber path for the first layer, $\langle T_0, T_1 \rangle^1$, remains consistent across manufacturing strategies and structural theories for both the constrained and unconstrained cases, with the only exception being the constrained ESL-TE1 complete overlap solution. It is worth noting that the

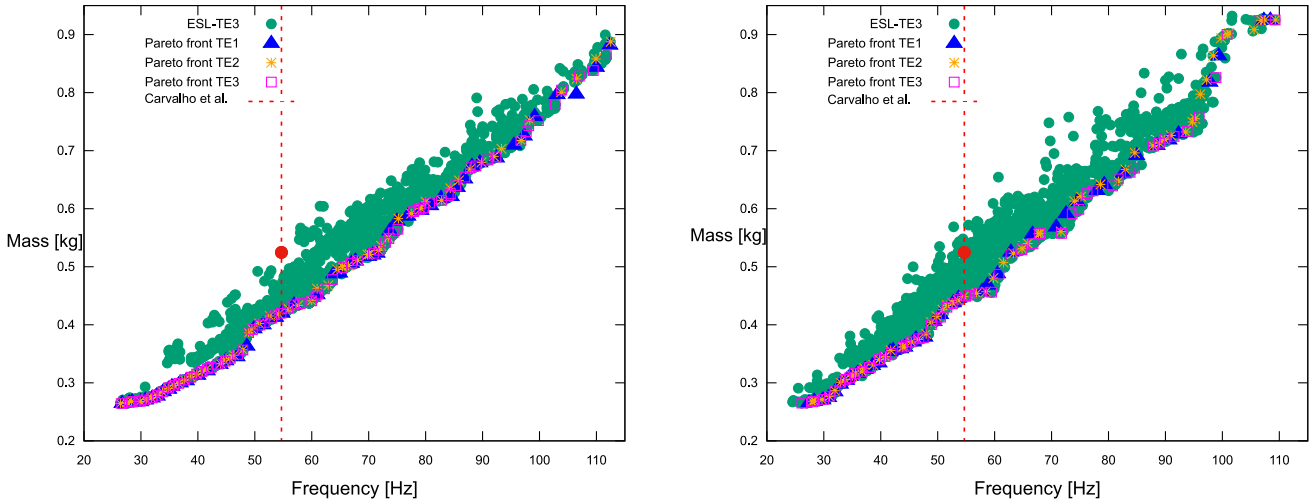

(a) Unconstrained Pareto front. (b) Constrained Pareto front

Fig. 14 Complete overlap Pareto fronts for the mass versus fundamental frequency optimization, illustrating the (**a**) unconstrained and (**b**) constrained cases. The results are derived using high-order ESL models to capture the influence of the structural theory

Table 8 Design results for the complete overlap unconstrained and constrained problems

	Unconstrained			Constrained		
	ESL-TE1	ESL-TE2	ESL-TE3	ESL-TE1	ESL-TE2	ESL-TE3
$\langle T_0, T_1 \rangle^1$ [°]	$\langle -89, -1 \rangle$	$\langle -89, -1 \rangle$	$\langle -89, -1 \rangle$	$\langle 88, 34 \rangle$	$\langle 89, 74 \rangle$	$\langle 89, 74 \rangle$
$\langle T_0, T_1 \rangle^2$ [°]	$\langle 82, -11 \rangle$	$\langle 86, -35 \rangle$	$\langle 86, -35 \rangle$	$\langle -45, -24 \rangle$	$\langle 85, 36 \rangle$	$\langle 85, 36 \rangle$
$\langle T_0, T_1 \rangle^3$ [°]	$\langle -43, -18 \rangle$	$\langle 52, -12 \rangle$	$\langle 52, -30 \rangle$	$\langle 62, 31 \rangle$	$\langle 70, 45 \rangle$	$\langle 70, 44 \rangle$
f_1 [Hz]	$55.78^{+2.01\%}$	$55.60^{+1.68\%}$	$55.34^{+1.20\%}$	$55.05^{+0.70\%}$	$55.38^{+1.28\%}$	$55.36^{+1.24\%}$
mass [kg]	$0.4286^{-18.31\%}$	$0.4237^{-19.25\%}$	$0.4223^{-19.52\%}$	$0.4483^{-14.56\%}$	$0.4511^{-14.03\%}$	$0.4511^{-14.03\%}$

The superscripts indicate the relative differences compared to the optimal reference solution reported in Carvalho et al. (2022))

ESL-TE1 model, which resembles FSDT formulations commonly used in commercial software, exhibits limitations in accurately capturing transverse shear effects.

- The outermost layers dominate in bending problems like the first free vibration mode, while the innermost plies are dominated by shear components. In this regard, only high-order models can predict these shear components accurately and, ultimately, provide better optimal designs for the innermost layers. This is observed in the optimal results for the three manufacturing conditions, structural theories, and the unconstrained and constrained optimization problems investigated.
- For unconstrained optimizations, when defects are not considered, results show that a seven-layer VAT plate can achieve designs with fundamental frequencies equal to or higher than the optimal eight-layer straight-fiber baseline. Even when a complete gap strategy is applied, seven layers are sufficient to reach at least the optimal frequency of the straight-fiber laminate. Weight savings for these configurations range from 12.5% in the defect-free solution to 18.5% with the complete gap solution. Consequently, Figs. 11a and 13a display the optimal fiber orientations for the first four layers of the quasi-symmetrical laminate. In contrast, only six layers are needed for the complete overlap condition to achieve a natural frequency higher than the eight-layer straight-fiber reference, resulting in a 19.5% weight reduction. Figure 15a illustrates the optimal fiber orientations for the first three layers of this symmetrical laminate.
- When the constraint on fiber path curvature is applied, the complete overlap strategy is the only approach that enables a six-layer VAT plate to achieve a fundamental frequency higher than the eight-layer straight-fiber one. The fiber paths for the first three layers of this optimal symmetrical laminate are shown in Fig. 15b. In contrast, if defects are neglected or the complete gap strategy is used, eight layers are needed to reach a fundamental frequency above the baseline of 54.68 Hz. The optimum results for the seven-layer configuration are reported

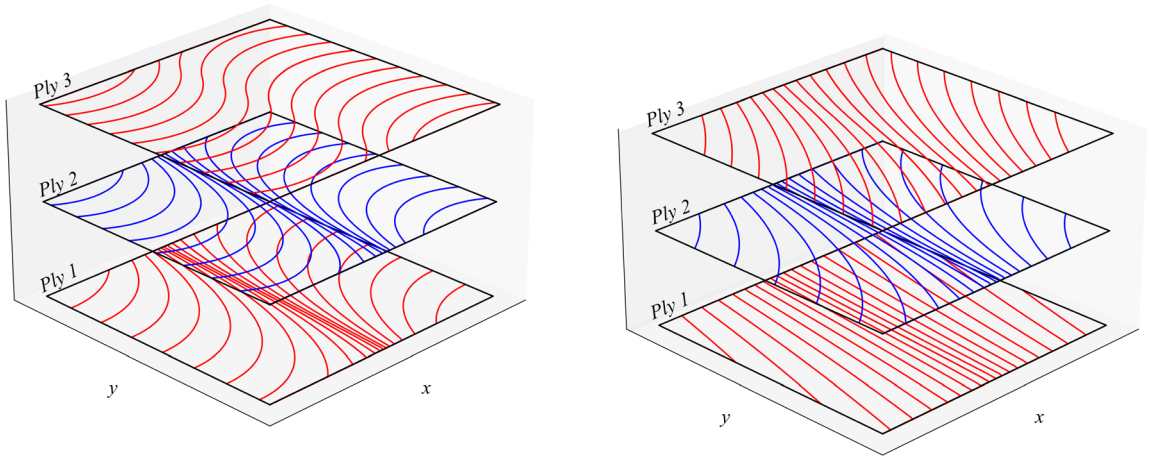

(a) Complete overlap unconstrained optimal fiber path

(b) Complete overlap constrained optimal fiber path

Fig. 15 Complete overlap unconstrained and constrained optimal fiber paths using ESL-TE3 structural theory, shown for half of the laminate due to its symmetric configuration

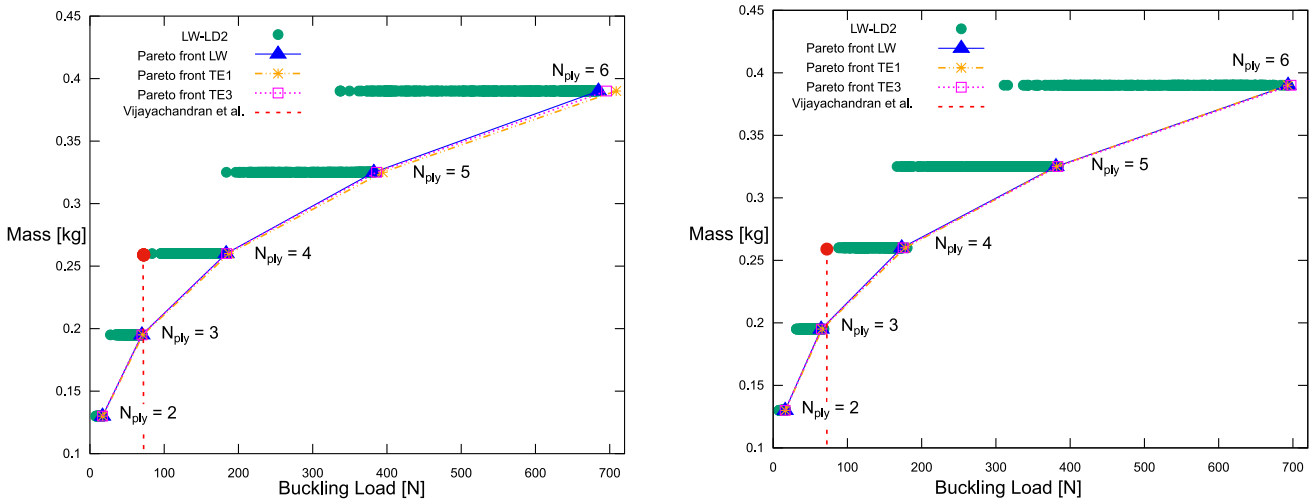

(a) Unconstrained Pareto front

(b) Constrained Pareto front

Fig. 16 Defect-free Pareto fronts for the mass versus buckling load optimization, illustrating the (**a**) unconstrained and (**b**) constrained cases. The results are derived using ESL and LW models to capture the influence of the structural theory

in Table 6 for the defect-free case and in Table 7 for the complete gap case to highlight the mass reduction relative to the reference case while maintaining a natural frequency below the baseline. Figures 11b and 13b show the optimal fiber trajectories for the first four layers in the defect-free and complete gap scenarios, respectively.

Table 9 Design results for the defect-free unconstrained and constrained problems

	Unconstrained			Constrained		
	ESL-TE1	ESL-TE3	LW-LD2	ESL-TE1	ESL-TE3	LW-LD2
$\langle T_0, T_1 \rangle^{1}$ [°]	$\langle -26, 58 \rangle$	$\langle 28, -59 \rangle$	$\langle 28, -59 \rangle$	$\langle 3, 49 \rangle$	$\langle -4, 44 \rangle$	$\langle -2, 44 \rangle$
$\langle T_0, T_1 \rangle^{2}$ [°]	$\langle -74, -45 \rangle$	$\langle 75, 44 \rangle$	$\langle 70, 44 \rangle$	$\langle -89, -36 \rangle$	$\langle -80, -41 \rangle$	$\langle -80, -41 \rangle$
N_{cr} [N]	$71.32^{-1.38\%}$	$69.93^{-3.30\%}$	$69.93^{-3.30\%}$	$65.92^{-8.85\%}$	$64.88^{-10.29\%}$	$64.65^{-10.60\%}$
mass [kg]	$0.1950^{-25.00\%}$	$0.1950^{-25.00\%}$	$0.1950^{-25.00\%}$	$0.1950^{-25.00\%}$	$0.1950^{-25.00\%}$	$0.1950^{-25.00\%}$

The superscripts indicate the relative differences compared to the reference solution reported in Vijayachandran et al. (2020)

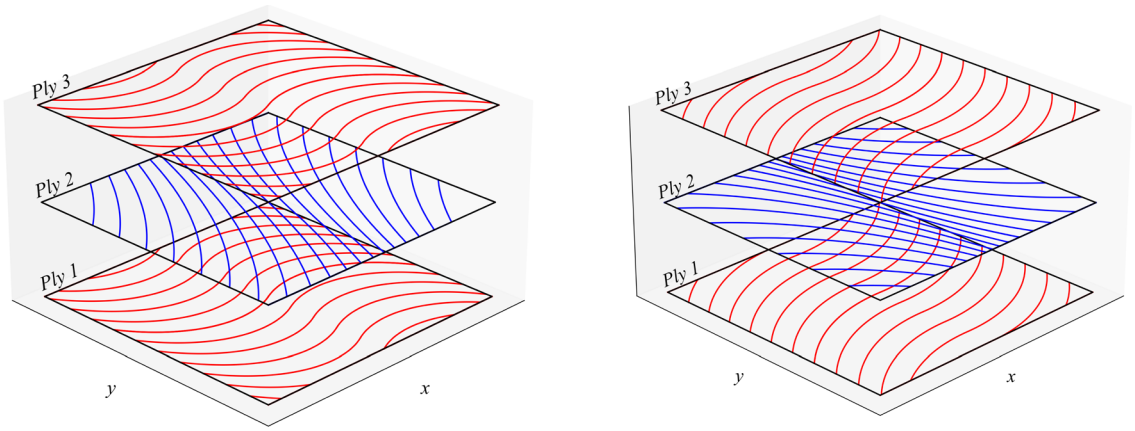

(a) Defect-free unconstrained optimal fiber path (b) Defect-free constrained optimal fiber path

Fig. 17 Defect-free unconstrained and constrained optimal fiber path using LW-LD2 structural theory

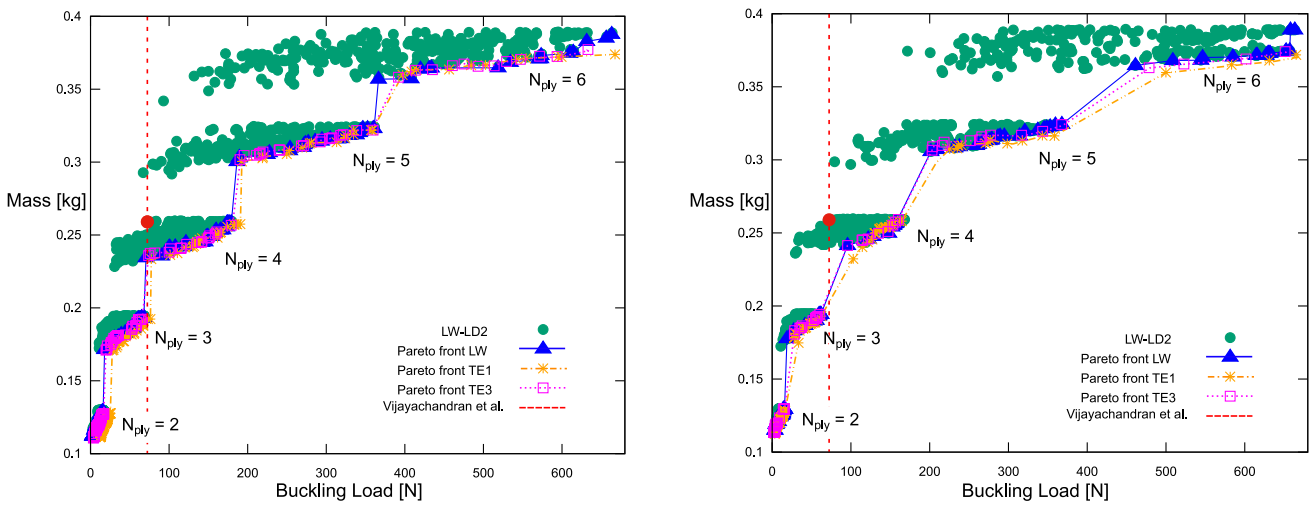

(a) Unconstrained Pareto front (b) Constrained Pareto front

Fig. 18 Complete gap Pareto fronts for the mass versus buckling load optimization, illustrating the (**a**) unconstrained and (**b**) constrained cases. The results are derived using ESL and LW models to account for the influence of the structural theory

Table 10 Design results for the complete gap unconstrained and constrained problem

	Unconstrained			Constrained		
	ESL-TE1	ESL-TE3	LW-LD2	ESL-TE1	ESL-TE3	LW-LD2
$\langle T_0, T_1 \rangle^{1}$ [°]	$\langle 32, -55 \rangle$	$\langle 20, -47 \rangle$	$\langle 26, -60 \rangle$	$\langle 6, -38 \rangle$	$\langle 4, 48 \rangle$	$\langle 5, 43 \rangle$
$\langle T_0, T_1 \rangle^{2}$ [°]	$\langle 60, 58 \rangle$	$\langle 64, 37 \rangle$	$\langle 77, 37 \rangle$	$\langle 72, 35 \rangle$	$\langle -59, -39 \rangle$	$\langle -58, -44 \rangle$
N_{cr} [N]	$67.84^{-6.19\%}$	$65.31^{-9.69\%}$	$65.01^{-10.11\%}$	$62.06^{-14.19\%}$	$60.45^{-16.41\%}$	$60.37^{-16.52\%}$
mass [kg]	$0.1916^{-26.31\%}$	$0.1913^{-26.42\%}$	$0.1909^{-26.58\%}$	$0.1922^{-26.05\%}$	$0.1920^{-26.16\%}$	$0.1919^{-26.20\%}$

The superscript indicates the relative difference with respect to the reference solution from v

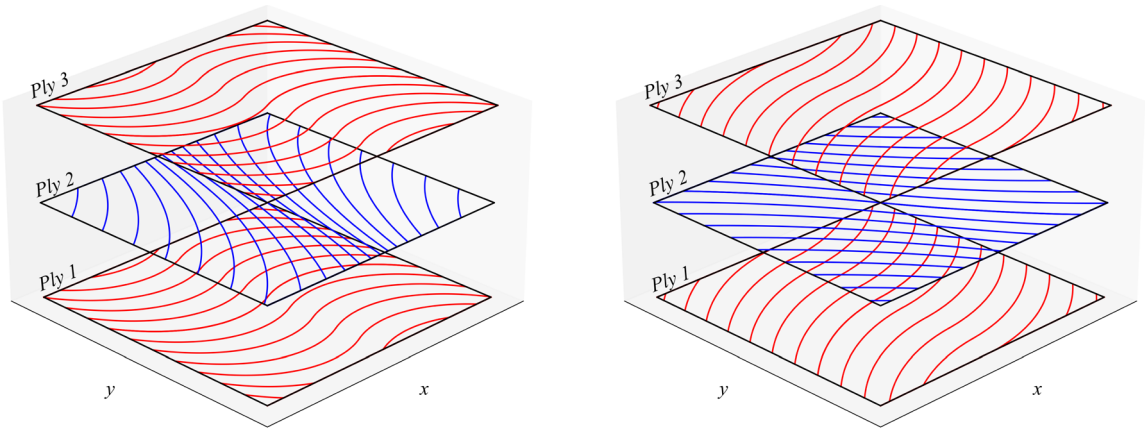

(a) Complete gap unconstrained optimal fiber path **(b)** Complete gap constrained optimal fiber path

Fig. 19 Complete gap unconstrained and constrained optimal fiber path using LW-LD2 structural theory

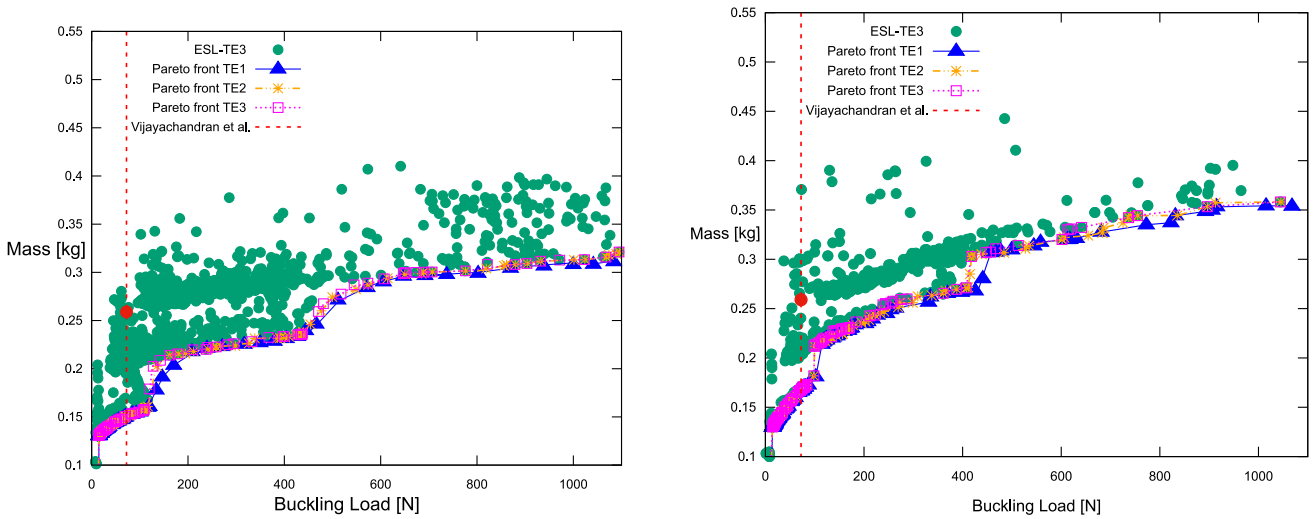

(a) Unconstrained Pareto front. **(b)** Constrained Pareto front

Fig. 20 Complete overlap Pareto fronts for the mass versus buckling load optimization, illustrating the (**a**) unconstrained and (**b**) constrained cases. The results are derived using high-order ESL models to capture the influence of the structural theory

Table 11 Design results for the complete overlap unconstrained and constrained problem

	Unconstrained			Constrained		
	ESL-TE1	ESL-TE2	ESL-TE3	ESL-TE1	ESL-TE2	ESL-TE3
$\langle T_0, T_1 \rangle$ [1] [°]	$\langle 48, -77 \rangle$	$\langle 48, -78 \rangle$	$\langle 49, -78 \rangle$	$\langle -19, -62 \rangle$	$\langle -18, -62 \rangle$	$\langle -17, -63 \rangle$
N_{cr} [N]	$83.74^{+15.79\%}$	$81.85^{+13.18\%}$	$81.82^{+13.14\%}$	$74.82^{+3.46\%}$	$73.62^{+1.80\%}$	$73.55^{+1.70\%}$
mass [kg]	$0.1527^{-41.02\%}$	$0.1526^{-41.05\%}$	$0.1526^{-41.05\%}$	$0.1686^{-35.10\%}$	$0.1686^{-35.10\%}$	$0.1686^{-35.10\%}$

The superscript indicates the relative difference with respect to the reference solution from Vijayachandran et al. (2020)

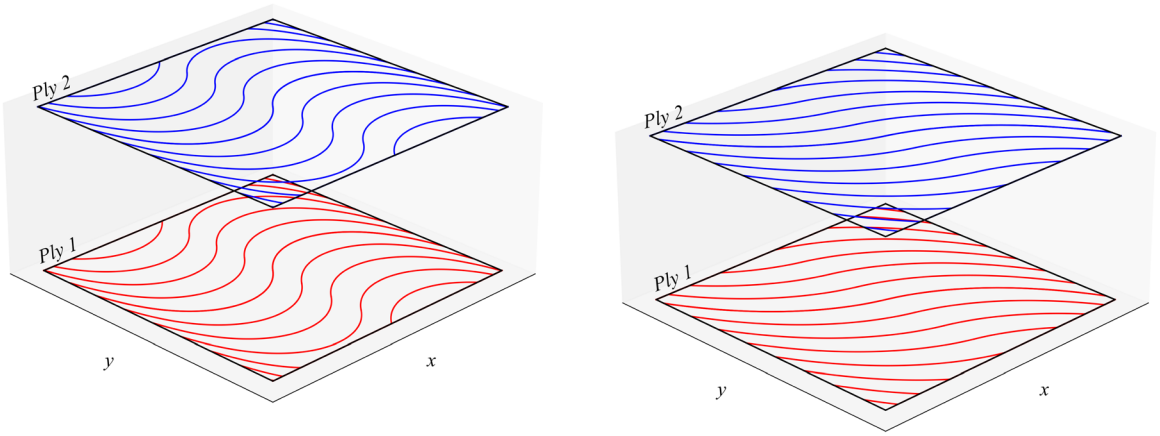

(a) Complete overlap unconstrained optimal fiber path

(b) Complete overlap constrained optimal fiber path

Fig. 21 Complete overlap unconstrained and constrained optimal fiber path using ESL-TE3 structural theory

5.2.2 Mass versus buckling load optimization

The second optimization problem under investigation is a VAT plate's mass versus buckling load. In this case, the squared plate presented by Vijayachandran et al. (2020) whose dimensions are $a = b = 0.508$ m, comprises four plies of individual thickness 0.19 mm and is subject to a uniaxial loading condition. In this optimization problem, the number of plies N_{ply} can vary discretely between two and six, and a symmetric stacking sequence is considered. At the same time, the lamination angles T_0 and T_1 for each ply can vary continuously between −90° and +90°. The objective is to minimize the mass while maximizing the critical buckling load.

The optimization results are compared to those present in Vijayachandran et al. (2020), where Bézier curves were employed to generate the varying fiber paths of each independent layer. That work reports a four-layered symmetric laminate. Thus, its design space was related to only two layers. The present work compares its outcomes against the optimal solution by Vijayachandran et al. (2020), which has a buckling load equal to 72.32 N (16.25 lb) and a mass of 0.284 kg (0.6265 lb). This solution was modeled through S4R Abaqus shell elements and is referred to as Design 1 in Vijayachandran et al. (2020).

Figure 16 shows the Pareto fronts of the defect-free manufacturing strategy and various structural models for the unconstrained and manufacture-constrained optimizations. Table 9 lists the stacking sequence retrieved for the optimal three-layered design, and Fig. 17 illustrates the optimal fiber paths for the defect-free scenario utilizing an LW-LD2 structural theory. For the mass versus buckling load optimization case, the fiber paths of the entire laminate are represented, despite its symmetric configuration, due to the lower number of layers involved. The Pareto fronts of the complete gap condition are available in Fig. 18, and the corresponding three-layered quasi-symmetric optimal designs are presented in Table 10. The LW-LD2 optimal fiber paths under these fabrication conditions are shown in Fig. 19. Finally, the complete overlap Pareto front is displayed in Fig. 20,

highlighting the influence of the chosen structural model on the results. The two-layered optimal designs are listed in Table 11, and the optimal fiber paths for the complete overlap strategy, obtained using the ESL-TE3 structural theory, are illustrated in Fig. 21. Note that the green dots in the Pareto fronts correspond to those evaluated with an LW-LD2 structural model for the defect-free and complete gap strategies, and to the designs evaluated with an ESL-TE3 in the case of complete overlap. The designs of the low-order ESL theories are not represented for the sake of clearness.

From the results outlined, the following can be stated:

- The discrete nature of the optimization problem is again appreciated, especially in the complete gap strategy Pareto fronts from Fig. 18 compared to those in Fig. 12.
- Again, it is observed that the structural theory has a weak influence in the defect-free optimal designs, as appreciated in Table 9. However, discrepancies are more evident when considering low-order kinematics like ESL-TE1. This difference is present in the optimal lamination angle for the second layer $\langle T_0, T_1 \rangle^2$ for both the unconstrained and constrained problems. Further, the ESL-TE1 constrained solution presents a different $\langle T_0, T_1 \rangle^1$ fiber path trend for the first layer compared to its ESL-TE3 and LW-LD2 counterparts. These differences are due to the inadequacy of low-order kinematic assumptions in capturing the three-dimensional stress distribution, especially in the presence of multimaterial configurations generated by the DLM. In particular, the ESL-TE1 model fails to accurately represent the transverse stress field required for the correct assembly of the geometric stiffness matrix. As a result, variations appear in both the optimal fiber path and the predicted buckling performance when compared to higher order models such as ESL-TE3 and LW-LD2.
- For both unconstrained and constrained optimizations, when defects are not considered, results indicate that a four-layer VAT plate can achieve critical buckling loads equal to or higher than the optimal four-layer baseline. Likewise, when a complete gap strategy is applied, at least four layers are needed to match the optimal buckling load reported in Vijayachandran et al. (2020). The optimal results for the three-layer configuration emphasize the mass reduction compared to the reference case despite showing a slight decrease in maximum buckling load compared to the baseline. Weight savings range from 25% in the defect-free solution to 26% with the complete gap solution. Figures 17 and 19 display the optimal fiber orientations for the optimal quasi-symmetrical three-layered laminate in the defect-free and complete gap scenarios, respectively.
- In contrast, the complete overlap strategy is the only approach that enables a two-layer VAT plate to achieve a buckling load higher than the reference, resulting in a 41% weight reduction for the unconstrained problem and a 35% reduction for the constrained problem. Figure 21 depicts the optimal fiber orientations for the symmetric two-layered laminate in both the unconstrained and constrained cases.

6 Conclusions

This paper presented a discrete, multi-objective, layerwise optimization framework for tow-steered composites, which generates discontinuous response surfaces and enables independent simulation of defects in each layer. The structural analyses were performed through an in-house CUF-based FE solver. CUF was used because of its versatility in generating different structural models without remeshing or rewriting the governing equations of the structural problem. Manufacturing defects, namely gaps and overlaps, have been modeled following the DLM, which modified the input files needed for the FEA depending on the manufacturing strategy, i.e., complete gap or complete overlap. Based on the results present in this manuscript, the following conclusions can be made:

- The discrete nature of the mass optimization problem necessitates a multi-objective heuristic algorithm, where an additional objective function is linked to the optimized structural performance. In this work, alongside minimizing mass, the goal was to maximize the fundamental frequency or the buckling load, focusing on achieving values above a specified threshold. Thus, the second objective was defined as one of these performance metrics. Achieving the desired structural performance requires adjustments to the stacking sequence across layers. Since the ply angles are continuous variables, while the number of layers is discrete, the resulting optimization problem becomes a mixed-integer one.
- Heuristic optimization approaches rely on an initial sampling to generate subsequent generations. In a single-objective heuristic algorithm, early generations often explore fiber path combinations for a fixed number of plies, typically fewer than the optimal solution. This limitation prevents the algorithm from producing values that surpass those of the reference. Consequently, a multi-objective approach is essential to adequately explore the design space and identify configurations with superior performance.
- For the defect-free manufacturing strategy, the choice of structural theory showed minimal impact on the Pareto fronts and the non-dominated design solutions for a fixed number of plies, as illustrated in Figs. 10 and 16. This effect was consistent across both unconstrained and curvature-constrained cases for the two least-weight optimization problems investigated (see Tables 6 and 9).

- In the least-weight versus fundamental frequency optimization problem, the different manufacturing strategies led to similar optimum fiber paths regardless of the structural theory, as shown in Table 6. The only difference between designs happened when defects were considered in the design optimization process. Specifically, complete gap optimal solutions presented defect regions in the edges of the plate (see Table 7), whereas in complete overlap optimal designs, the overlapping courses occur at the center of the plate (see Table 8).
- The study demonstrated that the choice of manufacturing strategy and structural theory significantly impacts the optimal solutions for the least-weight versus buckling optimization problem. This effect was particularly pronounced when the complete gap strategy was investigated, as seen in Table 10. This fabrication approach generates a multimaterial plate model during the simulation, requiring accurate stress predictions to compute the buckling load. In such cases, low-order kinematics, such as ESL-TE1 (similar to the well-known FSDT), fail to accurately predict the stress tensor, thereby affecting the identification of the optimal design. Therefore, the use of high-order structural models becomes essential when optimizing in the presence of manufacturing defects.

In conclusion, the proposed framework presents distinct advantages for the design of tow-steered laminates with manufacturing imperfections. Key strengths include directly integrating manufacturing defects (such as AFP-induced gaps/overlaps) into the optimization loop, enabling more realistic performance predictions. The layerwise formulation provides the possibility to model these defects independently at the ply level, while the discrete treatment of ply counts ensures physically meaningful designs. Furthermore, employing the CUF facilitates consistent and rigorous comparisons across different structural theories without remeshing. Conversely, the framework has limitations primarily related to computational demand. Using high-fidelity structural models, particularly for simulating thick laminates, significantly increases computational cost. In addition, preserving the discrete nature of the optimization problem, essential for layerwise defect modeling, necessitates using a heuristic algorithm. While this approach maintains high fidelity to the physical problem, it inherently incurs longer runtimes. Future investigations will aim to extend the proposed framework to account for uncertainty in defect distribution and material properties. This includes integrating multiscale stochastic variability with deterministic manufacturing. High-order structural theories will be essential to adequately capture their effects on structural performance and enable robust design optimization.

Author contributions D. Zamani: conceptualization, investigation, visualization, methodology, and writing—original draft preparation. A. Racionero Sánchez-Majano: conceptualization, investigation, visualization, methodology, and writing—original draft preparation. A. Pagani: supervision, software, writing—review and editing, funding acquisition, and conceptualization.

Funding This work is part of a project that has received funding from the European Research Council (ERC) under the European Union's Horizon 2020 research and innovation program (Grant Agreement No. 850437). The support of the Italian Ministry of University and Research through the program FARE-III Edition (project LOUD, No. R20EENHZEJ) is also acknowledged.

Data availability Data will be made available on request.

Declarations

Conflict of interest The authors declare that they have no conflict of interest.

References

Akbarzadeh AH, Arian Nik M, Pasini D (2014) The role of shear deformation in laminated plates with curvilinear fiber paths and embedded defects. Compos Struct 118:217–227. https://doi.org/10.1016/j.compstruct.2014.07.027

An H, Zhang Y, Deng Q, Long T, Youn BD, Kim HS (2025) Integrated optimization of ply number, layer thickness, and fiber angle for variable-stiffness composites using dynamic multi-fidelity surrogate model. Thin-Walled Struct 206:112392. https://doi.org/10.1016/j.tws.2024.112392

Arian Nik M, Fayazbakhsh K, Pasini D, Lessard L (2012) Surrogate-based multi-objective optimization of a composite laminate with curvilinear fibers. Compos Struct 94:2306–2313. https://doi.org/10.1016/j.compstruct.2012.03.021

Arian Nik M, Fayazbakhsh K, Pasini D, Lessard L (2014) Optimization of variable stiffness composites with embedded defects induced by automated fiber placement. Compos Struct 107:160–166. https://doi.org/10.1016/j.compstruct.2013.07.059

Blom AW, Lopes CS, Kromwijk PJ, Gurdal Z, Camanho PP (2009) A theoretical model to study the influence of tow-drop areas on the stiffness and strength of variable-stiffness laminates. J Compos Mater 43:403–425. https://doi.org/10.1177/0021998308097675

Borwankar P, Zhao W, Kapania RK, Bansal M (2022) Two-level weight optimization of composite laminates using integer programming. AIAA J 60:6436–6446. https://doi.org/10.2514/1.J061560

Borwankar P, Zhao W, Kapania RK, Bansal M (2023) Optimization of hybrid composite laminates with distinct ply thicknesses using integer programming. AIAA J 61:5609–5619. https://doi.org/10.2514/1.J062488

Brasington A, Sacco C, Halbritter J, Wehbe R, Harik R (2021) Automated fiber placement: a review of history, current technologies, and future paths forward. Compos Part C Open Access 6:100182. https://doi.org/10.1016/j.jcomc.2021.100182

Brooks TR, Martins J (2018) On manufacturing constraints for tow-steered composite design optimization. Compos Struct 204:548–559. https://doi.org/10.1016/j.compstruct.2018.07.100

Carrera E (1997) CZ0 requirements: models for the two dimensional analysis of multi-layered structures. Compos Struct 37:373–383. https://doi.org/10.1016/S0263-8223(98)80005-6

Carrera E (2002) Theories and finite elements for multilayered, anisotropic, composite plates and shells. Arch Comput Methods Eng 9:87–140. https://doi.org/10.1007/BF02736649

Carrera E, Cinefra M, Petrolo M, Zappino E (2014) Finite element analysis of structures through unified formulation. Hoboken, New Jersey

Carvalho J, Sohouli A, Suleman A (2022) Fundamental frequency optimization of variable angle tow laminates with embedded gap defects. J Compos Sci 6:64. https://doi.org/10.3390/jcs6020064

Deb K (2001) Multi-objective optimization using evolutionary algorithms. Chichester

Demasi L, Biagini G, Vannucci F, Santarpia E, Cavallaro R (2017) Equivalent single layer, zig-zag, and layer wise theories for variable angle tow composites based on the generalized unified formulation. Compos Struct 177:54–79. https://doi.org/10.1016/j.compstruct.2017.06.033

Ding H, Xu B, Li W, Huang X (2022) Design of curvilinear variable-stiffness composites considering stiffness, strength and manufacturability. Struct Multidiscip Optim. https://doi.org/10.1007/s00158-022-03306-w

Fayazbakhsh K, Arian Nik M, Pasini D, Lessard L (2013) Defect layer method to capture effect of gaps and overlaps in variable stiffness laminates made by automated fiber placement. Compos Struct 97:245–251. https://doi.org/10.1016/j.compstruct.2012.10.031

Ghayour M, Hojjati M, Ganesan R (2021) Induced defect layer method to characterize the effect of fiber tow gaps for the laminates manufactured by automated fiber placement technique. J Compos Mater 55:4011–4027. https://doi.org/10.1177/00219983211031649

Groh RM, Weaver P (2015) Mass optimisation of variable angle tow, variable thickness panels with static failure and buckling constraints. In: 56th AIAA/ASCE/AHS/ASC structures, structural dynamics, and materials conference. https://doi.org/10.2514/6.2015-0452

Gurdal Z, Olmedo R (1993) In-plane response of laminates with spatially varying fiber orientations–variable stiffness concept. AIAA J 31:751–758. https://doi.org/10.2514/3.11613

Gürdal Z, Tatting BF, Wu CK (2008) Variable stiffness composite panels: effects of stiffness variation on the in-plane and buckling response. Compos A Appl Sci Manuf 39:911–922. https://doi.org/10.1016/j.compositesa.2007.11.015

Harik R, Saidy C, Williams S, Gurdal Z, Grimsley B (2018) Automated fiber placement defect identity cards: cause, anticipation, existence, significance, and progression. In: Proceedings of the SAMPE 2018 conference & exhibition, Long Beach

Heinecke F, Willberg C (2019) Manufacturing-induced imperfections in composite parts manufactured via automated fiber placement. J Compos Sci 3:56. https://doi.org/10.3390/jcs3020056

Izzi MI, Catapano A, Montemurro M (2021) Strength and mass optimisation of variable-stiffness composites in the polar parameters space. Struct Multidiscip Optim 64:2045–2073. https://doi.org/10.1007/s00158-021-02963-7

Jaber A, Lafon P, Younes R (2021) A branch-and-bound algorithm based on NS-GAII for multi-objective mixed integer nonlinear optimization problems. Eng Optim 54:1004–1022. https://doi.org/10.1080/0305215X.2021.1904918

Kim BC, Potter K, Weaver PM (2012) Continuous tow shearing for manufacturing variable angle tow composites. Compos A Appl Sci Manuf 43:1347–1356. https://doi.org/10.1016/j.compositesa.2012.02.024

Kim BC, Weaver PM, Potter K (2014) Manufacturing characteristics of the continuous tow shearing method for manufacturing of variable angle tow composites. Compos Part A Appl Sci Manuf 61:141–151. https://doi.org/10.1016/j.compositesa.2014.02.019

Lozano GG, Tiwari A, Turner C, Astwood S (2015) A review on design for manufacture of variable stiffness composite laminates. Proc Inst Mech Eng Part B Eng Manuf 230:981–992. https://doi.org/10.1177/0954405415600012

Lukaszewicz DH-JA, Ward C, Potter K (2012) The engineering aspects of automated prepreg layup: history, present and future. Compos B Eng 43:997–1009. https://doi.org/10.1016/j.compositesb.2011.12.003

Montemurro M, Catapano A (2016) A new paradigm for the optimum design of variable angle tow laminates. In: Variational analysis and aerospace engineering: mathematical challenges for the aerospace of the future. Cham, pp 375–400. https://doi.org/10.1007/978-3-319-45680-5_14

Montemurro M, Catapano A (2017) On the effective integration of manufacturability constraints within the multi-scale methodology for designing variable angle-tow laminates. Compos Struct 161:145–159. https://doi.org/10.1016/j.compstruct.2016.11.018

Montemurro M, Mas A, Zerrouq SE (2024) Topology and anisotropy optimisation of continua using non-uniform rational basis spline entities. Comput Methods Appl Mech Eng 420:116714. https://doi.org/10.1016/j.cma.2023.116714

Nardin L, Sárensen K, Hitzel S, Tremel U (2009) modeFRONTIER, a framework for the optimization of military aircraft configurations. In: Kroll N, Schwamborn D, Becker K, Rieger H, Thiele F (eds) MEGADE-SIGN and MegaOpt—German Initiatives for aerodynamic simulation and optimization in aircraft design, Berlin, pp 191–205. https://doi.org/10.1007/978-3-642-04093-1_14

Nguyen MH, Vijayachandran AA, Davidson P, Call D, Lee D, Waas AM (2019) Effect of automated fiber placement (AFP) manufacturing signature on mechanical performance of composite structures. Compos Struct 228:111335. https://doi.org/10.1016/j.compstruct.2019.111335

Nguyen MH, Vijayachandran AA, Davidson P, Call D, Lee D, Waas AM (2019b) Effect of automated fiber placement (AFP) manufacturing signature on mechanical performance. In: AIAA Scitech 2019 Forum. https://doi.org/10.2514/6.2019-0516

Ntourmas G, Glock F, Daoud F, Schuhmacher G, Chronopoulos D, Ozcan E (2021) Mixed integer linear programming formulations of the stacking sequence and blending optimisation of composite structures. Compos Struct 264:113660. https://doi.org/10.1016/j.compstruct.2021.113660

Pagani A, Azzara R, Carrera E (2022) Geometrically nonlinear analysis and vibration of in-plane-loaded variable angle tow composite plates and shells. Acta Mech 234:85–108. https://doi.org/10.1080/15376494.2020.1771485

Pagani A, Petrolo M, Sáanchez-Majano AR (2023) Stochastic characterization of multiscale material uncertainties on the fibre-matrix interface stress state of composite variable stiffness plates. Int J Eng Sci 183:103787. https://doi.org/10.1016/j.ijengsci.2022.103787

Pagani A, Racionero Sánchez-Majano A, Zamani D, Petrolo M, Carrera E (2024) Fundamental frequency layer-wise optimization of tow-steered composites considering gaps and overlaps. Aerotecnica Missili Spazio. https://doi.org/10.1007/s42496-024-00212-w

Pagani A, Racionero Sánchez-Majano A, Zamani D (2024b) Optimization of variable stiffness composites considering gaps/overlaps and unified structural theories. In: ASME aerospace structures, structural dynamics, and materials conference, p 87745. https://doi.org/10.1115/SSDM2024-121550

Racionero Sánchez-Majano A, Pagani A (2023) Buckling and fundamental frequency optimization of tow-steered composites using layerwise structural models. AIAA J 61:4149–4163. https://doi.org/10.2514/1.J062976

Reddy JN (2004) Mechanics of laminated composite plates and shells: theory and analysis. Boca Raton, Florida

Rousseau G, Wehbe R, Halbritter J, Harik R (2018) Automated fiber placement path planning: a state-of-the-art review. Comput Aided Design Appl 16:172–203. https://doi.org/10.14733/cadaps.2019.172-203

Sáanchez-Majano AR, Azzara R, Pagani A, Carrera E (2021) Accurate stress analysis of variable angle tow shells by high-order equivalent-single-layer and layer-wise finite element models. Materials 14:6486. https://doi.org/10.3390/ma14216486

Sáanchez-Majano AR, Pagani A, Petrolo M, Zhang C (2021) Buckling sensitivity of tow-steered plates subjected to multiscale defects by high-order finite elements and polynomial chaos expansion. Materials 14:2706. https://doi.org/10.3390/ma14112706

Tian Y, Pu S, Zong Z, Shi T, Xia Q (2019) Optimization of variable stiffness laminates with gap-overlap and curvature constraints. Compos Struct 230:111494. https://doi.org/10.1016/j.compstruct.2019.111494

Urso E, Montemurro M (2024) On thermomechanical problems in a topology optimisation method based on non-uniform rational basis spline entities. Comput Struct 305:107530. https://doi.org/10.1016/j.compstruc.2024.107530

Urso E, Zerrouq SE, Montemurro M (2023) A topology optimization method for problems with design-dependent loads based on non-uniform rational basis spline entities. Mech Adv Mater Struct 31:10671–10686. https://doi.org/10.1080/15376494.2023.2294495

Viglietti A, Zappino E, Carrera E (2019) Analysis of variable angle tow composites structures using variable kinematic models. Compos B Eng 171:272–283. https://doi.org/10.1016/j.compositesb.2019.03.072

Vijayachandran AA, Davidson P, Waas AM (2020) Optimal fiber paths for robotically manufactured composite structural panels. Int J NonLinear Mech 126:103567. https://doi.org/10.1016/j.ijnonlinmec.2020.103567

Wu B, Pagani A, Chen WQ, Carrera E (2019) Geometrically nonlinear refined shell theories by Carrera unified formulation. Mech Adv Mater Struct 28:1721–1741. https://doi.org/10.1080/15376494.2019.1702237

Zhang L, Wang X, Pei J, Zhou Y (2020) Review of automated fibre placement and its prospects for advanced composites. J Mater Sci 55:7121–7155. https://doi.org/10.1007/s10853-019-04090-7